Large-scale Biaxial Friction Experiments Using a NIED Large-scale Shaking Table

– Design of Apparatus and Preliminary Results –

Eiichi FUKUYAMA[*1], Kazuo MIZOGUCHI[*2,a], Futoshi YAMASHITA[*1], Tetsuhiro TOGO[*1,b],
Hiroyuki KAWAKATA[*3,a], Nana YOSHIMITSU[*3,c], Toshihiko SHIMAMOTO[*4],
Tadashi MIKOSHIBA[*1], Makoto SATO[*5], Chikahiro MINOWA[*6,a], Toshiyuki KANEZAWA[*6],
Hiroshi KUROKAWA[*6], and Toya SATO[*6]

*[*1] National Research Institute for Earth Science and Disaster Prevention, Japan*
fuku@bosai.go.jp
*[*2] Central Research Institute of Electric Power Industry, Japan*
*[*3] Ritsumeikan University, Japan*
*[*4] Institute of Geology, China Earthquake Administration, China*
*[*5] Advanced Engineering Service Co., Ltd., Japan*
*[*6] Tomoe Research & Development Co., Ltd., Japan*
[a] Visiting researcher of the National Research Institute for Earth Science and Disaster Prevention.
[b] Now at Institute of Geology, China Earthquake Administration
[c] Now at Earthquake Research Institute, the University of Tokyo

Abstract

To investigate the scale dependency of friction and the characteristics of dynamic rupture propagation, we developed a large-scale biaxial friction apparatus using the large-scale shaking table (15 m × 14.5 m) at the National Research Institute for Earth Science and Disaster Prevention in Japan. We carried out a series of large-scale friction experiments using this apparatus in the spring of 2012. In the apparatus, the actuators of the shaking table were used as the engine of the constant speed loading force applied to a pair of specimens made of Indian gabbro. A 1.5-m-long quadrangular prismatic specimen overlaid on a 2-m specimen was used. Their height and width were 0.5 m. The lower 2-m-long specimen moves with the shaking table and the upper 1.5-m-long specimen is fixed to the basement of the shaking table by a reaction force bar. The shaking table can generate a maximum displacement of 0.4 m with a velocity ranging between 0.025 mm/s and 1 m/s. Before the series of experiments, the sliding surface was flattened with less than 0.01 mm undulation using a large-scale surface grinder. However, the surface roughness evolved with the subsequent experiments. Normal stress was applied up to 1.3 MPa. The stiffness of this apparatus was measured experimentally and was of the order of 0.1 GN/m. We measured the coefficients of friction under a constant loading velocity between 0.025 and 100 mm/s. The coefficient of friction was about 0.75 under the normal stress between 0.13 and 1.3 MPa for the loading velocity of 0.1 mm/s and 1 mm/s. As the loading velocity increased, the coefficient of friction decreased. The obtained coefficient of friction was consistent with those obtained by previous studies using smaller specimens. We then monitored the stick-slip events by observing the shear stress change evolution measured by strain gauges as well as by the high-frequency wave emission measured by piezoelectric transducers. These sensors were attached at the edge of the slipping area. We found that there were many stick-slip events that nucleated inside the sliding surface but did not reach the edge of the sliding surface until the termination of slip. The locations of these high-frequency events correspond to the place where the slip was nucleated. We found that these locations were on the edge of the grooved surfaces that were created in the previous experiments.

Key words: Rock friction experiment, Large-scale biaxial friction apparatus, Coefficient of friction, Stick-slip events, Earthquake rupture propagation

---

[*1] 3-1 Tennodai, Tsukuba, Ibaraki, 305-0006, Japan
[*2] Abiko, Chiba, 270-1194, Japan
[*3] Kusatsu, Shiga, 525-8577, Japan
[*4] Beijing, 100-029, China
[*5] Tsukuba, Ibaraki, 305-0032, Japan
[*6] Chuo-ku, Tokyo, 104-0054, Japan

1. Introduction

Despite significant advances in the modeling of earthquake rupture propagation [e.g., Oglesby *et al.*, 1998; Aochi and Fukuyama, 2002; Fukuyama and Mikumo, 2006; Hok *et al.*, 2011], the dynamics of earthquake rupture in nature are not yet fully understood. Several models have been proposed to explain the nucleation of earthquake rupture [e.g., Dieterich, 1986; Ohnaka and Shen, 1999; Shibazaki and Matsu'ura, 1998; McLaskey and Kilgore, 2013; Latour *et al.*, 2013], but not all aspects of earthquake rupture nucleation have been explained consistently.

Recent advances in seismological observation networks have not sufficiently helped improve the imaging of rupture propagation because of insufficient resolution in the waveform inversion analysis [e.g., Koketsu *et al.*, 2011; Lay *et al.*, 2012]. These resolution problems might be intrinsic. It has been difficult to retrieve such information from seismological observations.

The size effects of the earthquake slip area could be important. To understand the dynamics of earthquake rupture at various scales, near-fault observations of earthquake faulting would be ideal, but such observations are not possible because the seismogenic zone where most earthquakes occur cannot be reached. Thus, to investigate rupture dynamics, experimental approaches have been taken using similar rock materials under environmental conditions similar to those of earthquakes. However, the size of rock specimens used in the laboratory and that of the rocks in natural earthquakes are quite different.

There have been many reports about the coefficient of friction under various conditions [e.g., Dieterich, 1972, 1978a, 1979, 1981; Byerlee, 1978; Ohnaka *et al.*, 1987; Marone, 1998; Reches and Lockner, 2010; Di Toro *et al.*, 2011; Goldsby and Tullis, 2011], but these reports were based mainly on centimeter-scale rock specimens measured in the laboratory - much smaller specimens than the faults observed in natural earthquakes. It is important to know whether a scale effect should be taken into account when extrapolating experimental results to natural earthquakes. Ohnaka and Shen [1999] proposed that surface roughness could be a scaling parameter for the extrapolation of experimental results, but this idea has not yet been experimentally confirmed, although some attempts were made to extract the scaling parameters from seismological observations [Guatteri and Spudich, 2000; Mikumo *et al.*, 2003; Fukuyama and Mikumo, 2007].

In such experiments, we need spatial resolution to resolve the details of the rupture propagation. Since the dimensions of the available sensors are of the order of millimeters, we need at least a meter-scale sample to get sufficient spatial resolution. A large friction apparatus was constructed to observe rupture propagation in the laboratory in which a 1.5-m-square block of Sierra Nevada granite with a thickness of 0.4 m cut along the diagonal line was used [Dieterich, 1978b; Dieterich *et al.*, 1978; Okubo and Dieterich, 1984; Beeler *et al.*, 2012; McLaskey and Kilgore, 2013]. The loading is applied to the rock specimens by four flat jacks. Since flat jacks are used as the loading devices, the slip displacement was not long enough to observe the evolution of the slip surface as a function of slip displacement.

To investigate the above two topics, i.e., the size dependency of friction and the rupture propagation of stick-slip events, we constructed a large-scale apparatus for friction experiments using the assistance of a shaking table facility. Shaking tables are designed to dynamically control the movement of the table as precisely as possible. With a conventional apparatus, a broad range of loading velocity up to seismic slip velocity and a large slip distance are difficult to achieve. The core of our system described herein is the servo-controlled oil actuator, which is the same as that used in the traditional friction apparatus systems. By using an existing shaking table, our large-scale apparatus was constructed at a very reasonable cost, and it demonstrated high performance.

Here we provide the detailed structure of our system and some of the preliminary results obtained with it. In February 2012, the first friction testing apparatus was constructed on the large-scale shaking table (hereafter referred to as G-1) at the National Research Institute for Earth Science and Disaster Prevention (NIED) in Tsukuba, Japan [see Minowa *et al.*, 1989 for the details of the shaking table]. In March 2013, several improvements were made to the G-1 and a revised apparatus was constructed (referred to as G-2). In this paper, we describe the details of G-1 and the results obtained with G-1; we will describe the details of G-2 and the corresponding results in the near future.

2. Design of Apparatus

2.1 General Design

A sort of sandwich-type configuration was employed for the friction testing apparatus. It has two sets of sliding surfaces, one of which is composed of a low-friction rail-roller system and the other is the surface contacted by two rock specimens. This configuration serves to minimize the amount of rock specimens needed. A 1.5-m-long quadrangular prismatic rock specimen overlaid on a 2-m specimen was used in the apparatus as shown in **Fig. 1**. The lower specimen is fixed to the shaking table floor and the upper specimen is sustained by the reaction force bar, which is fixed to the basement of the shaking table. Thus, as the shaking table moves, the shear force is applied to the two rock specimens and their interfaces dislocate.

The apparatus consists of four units: 1) the main body,
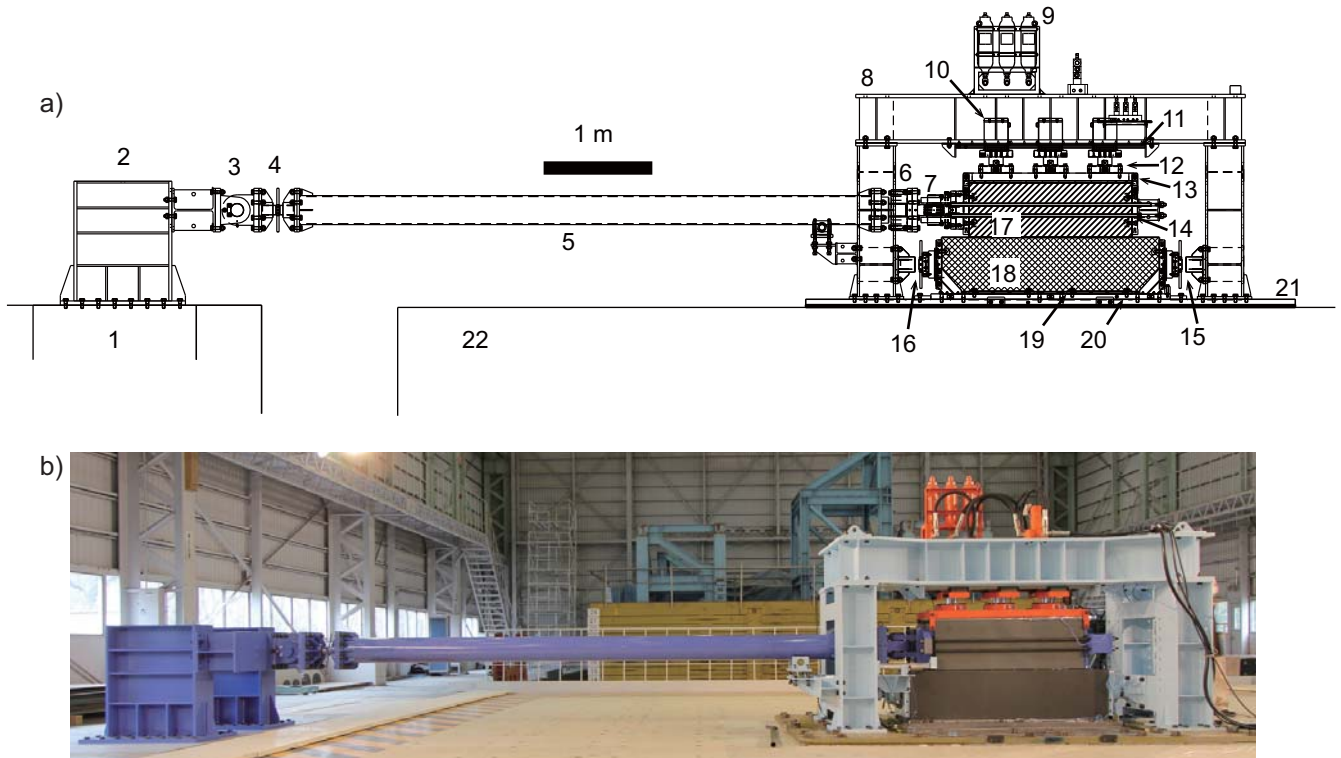
Fig. 1 a) The configuration of the apparatus. As the shaking table moves, the lower rock sample moves to the same degree, whereas the upper rock sample is fixed to the ground via a reaction force bar. The numerals in the figure show the parts of the apparatus as follows. **1:** basement for reaction force, **2:** reaction force horse, **3:** swivel for vertical adjustment, **4:** turn-buckle for the adjustment of the location of the upper specimen, **5:** reaction force bar, **6:** 1.2-MN load cell for the measurements of horizontal force, **7:** swivel for horizontal adjustment, **8:** four-legged main frame, **9:** three 0.4-L accumulators, **10:** three actuators, **11:** LM roller, **12:** three 0.4-MN load cell for the measurements of vertical force, **13:** upper sample plate, **14:** PC steel bars, **15 and 16:** turn-buckles to fix the lower specimen, **17:** upper specimen, **18:** lower specimen, **19:** lower sample plate, **20:** sliding table, **21:** base plate for the apparatus, **22:** shaking table. **b)** Overview photo of the apparatus.

2) the press system, 3) the reaction force system, and 4) the shaking table. The main body supports the normal force applied vertically to the rock specimens. The function of the press system is to apply the normal force to the specimens. The purpose of the reaction force system is to apply the shear force to the specimens by preventing the upper specimen from moving with the shaking table. Thus, the upper specimen is fixed to the ground and the lower specimen moves with the shaking table. The shaking table is the engine of the system to control the dislocation between the specimens. In the following, the numbers in parentheses refer to the parts shown in **Fig. 1**.

2.2 Main Body

The main body consists of a four-legged frame (8 and **Fig. 2**), a base plate (21 and **Fig. 3**), and equipment for the management of the specimens (**Figs. 4** and **5**).

The base plate (21), whose dimensions are 4.5 m × 2.5 m, is fixed on the shaking table floor by 2-inch bolts. It is quite important to adjust the direction of the movement of the rock specimen with respect to the reaction force bar. Thus,

the orientation of the base plate was precisely adjusted to the shaking direction of the shaking table within a misfit of 1 sec using the transit compass. In addition, the horizontal level of the base plate was accurately adjusted within 0.1-mm undulation to locate the plate as horizontally as possible. After the installation of the base plate, gaps between the base plate and the shaking table were thoroughly grouted to enable the base plate to support normal loads.

The four-legged frame (8 and **Fig. 2**) was then built on the base plate. The approximate size of the frame is 3.6 m long, 1.4 m wide and 1.9 m high. At the top of the frame, the pressure system is attached on the sliding plate. This sliding plate is placed above the upper rock specimen and connected to the frame by the linear movement (LM) roller.

The sample management equipment (**Fig. 4**) facilitates the installation and de-installation of the specimens before and after the experiments. It consists of a sliding table below the lower specimen, two turnbuckles (15, 16), PC steel bars (14), and a sliding table (20) connected to the frame via LM rollers (**Fig. 4**). The sliding table above the base plate that
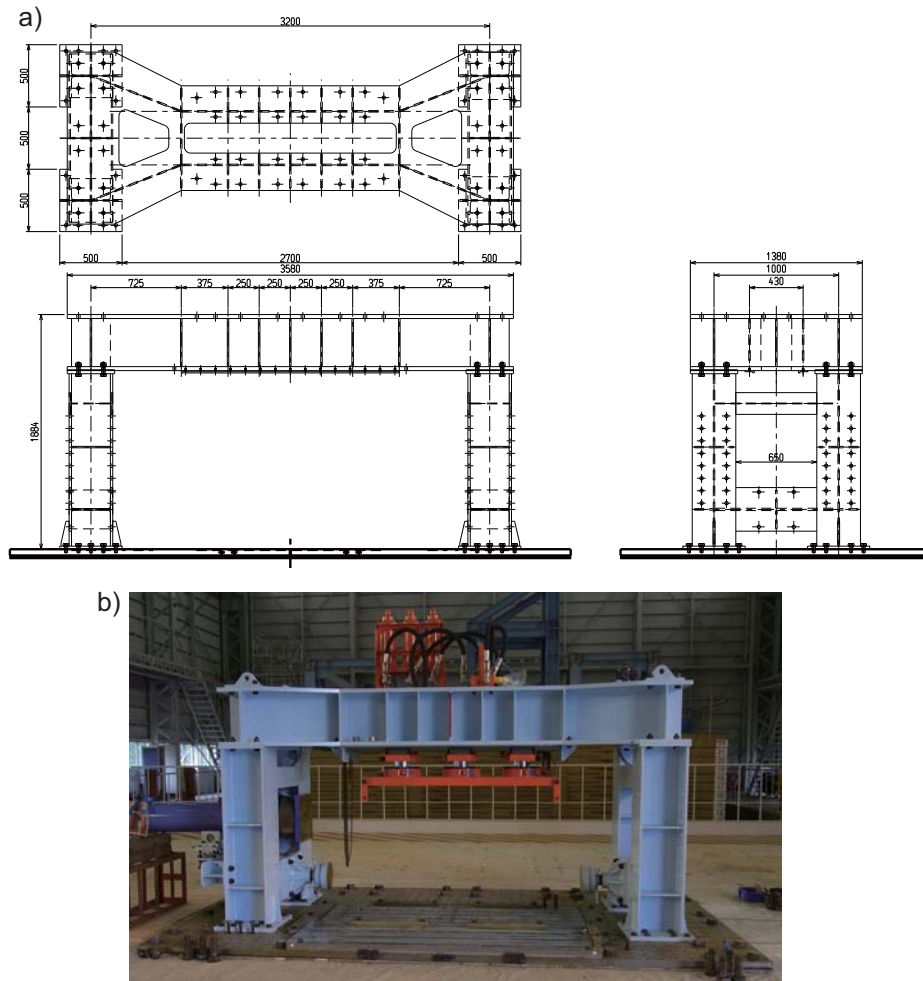
Fig. 2 Main frame of the apparatus. The four-legged press is fixed on the base plate located on the shaking table.
a) Sketch of the main frame. **b)** Photo of the main frame attached to the press system and reaction force bar.

moves perpendicular to the slip direction is used to insert the rock specimen into the apparatus and to take it out from the apparatus. The turnbuckles (15, 16) are used to fix the lower specimen. The PC steel bars (14) are used to apply confining force to the upper specimen. They support the tensional force when the shaking table moves in the opposite direction and enable the reverse slip experiments. This equipment markedly reduces the necessary preparation time for each run by its quick installation / de-installation mechanisms.

2.3 Press System

The press system consists of three actuators, each of which has a capacity of 0.4 MN as shown in **Fig. 6**. The pump supplies oil to pressurize the actuators until the target pressure is achieved. Once the pressure reaches the target value, the valve to the pump is closed in order to maintain uniform pressure during the experiment with a 0.4-L capacity accumulator attached to each actuator (12) (**Fig. 6**). These accumulators (9) in the closed oil circuit homogenize the pressure disturbance during the experiment.

Three independently controlled actuators enable us to

apply spatially variable vertical force to the rock specimens, which serves to spatially homogenize normal stress. The servo-controlled valves, which could not be introduced in the apparatus due to funding limitations, would serve to accurately maintain the uniform normal stress on the fault. Instead, three accumulators were attached to the actuators to stabilize the fluctuation of oil pressure caused by the displacement at the piston.

2.4 Reaction-force Support System

To generate displacements between the interfaces of two rock specimens, the lower specimen (18) is fixed to the shaking table (22) and the upper specimen (17) is fixed to the basement of the shaking table. To fix the upper rock sample to the basement, we constructed a reaction force support system. This system consists of a reaction force bar (5), a reaction force horse (2), and a reaction force base (1).

The base for the reaction force (1) had already been constructed as a part of the shaking table facility. The shear resistance of the base was roughly estimated at 1 MN by its structure (i.e., based on the thickness of the plate and the

a)

b)
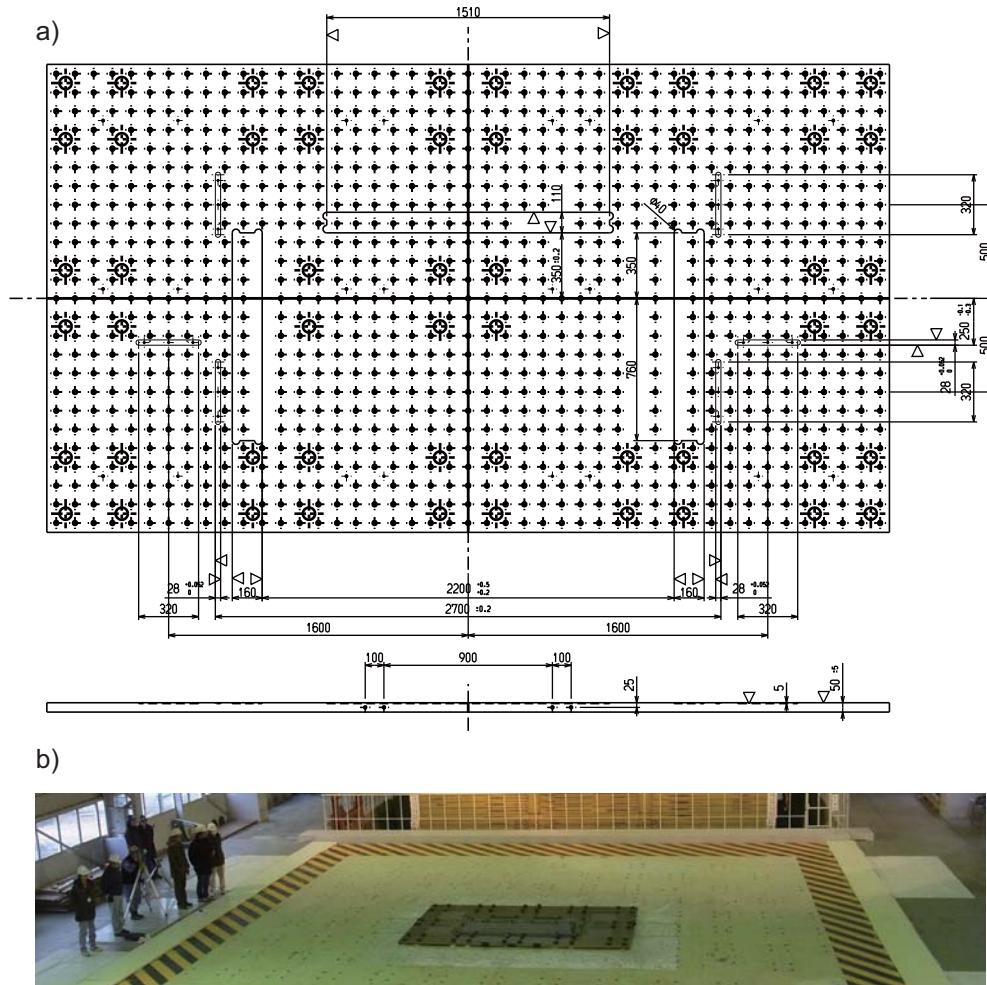
Fig. 3 Base plate of the apparatus. The base plate (21) is fixed to the shaking table by 2-inch bolts. The press was put on the base plate and connected by M24 bolts. **a)** Drawing of the base plate. **b)** Photo of the base plate.

number of bolts connected to the shaking table basement). This amount is considered to be the maximum value of normal force applied to the rock specimen, assuming that the coefficient of friction of rock is roughly 1. We thus designed the apparatus to support the maximum 1-MN reaction force generated by the shaking table via the rock friction.

The reaction force horse (2) is constructed above the reaction force base (1). It is important to adjust the orientation of the base (1) and the position of the center of the horse (2) to align the center of the base plate of the apparatus (20). Once the reaction force horse (2) is precisely set on the base (1), the reaction force bar (5) can connect both the reaction force horse (2) and an upper rock specimen (17) along a straight line parallel to the shaking table motion.

To adjust any tiny vertical misalignment, a vertical turnbuckle (3) is inserted between the reaction force horse (2) and the reaction force bar (5). In addition, a load cell (6) and a horizontal turnbuckle (7) are inserted between the reaction force bar (5) and the upper specimen (17) to adjust tiny horizontal misalignment and to measure the horizontal force,

as shown in **Figs. 1** and **7**.

2.5. Large-scale Shaking Table

The NIED large-scale shaking table consists of a 15 m × 14.5 m table, hydraulic support columns (four large columns and eight small columns), four actuators, and a concrete basement [Minowa *et al.*, 1989]. The motion of the shaking table is controlled by the displacement-based hydraulic servo-control system. The table moves in one horizontal direction. The maximum loading capacity is 4.9 MN, the maximum displacement is 440 mm, the maximum velocity is 1 m/s, and the maximum acceleration is 9.4 m/s^2 in the frequency range up to 50 Hz [Minowa *et al.*, 1989].

The base plate of the apparatus was fixed at the center of the table to sustain the apparatus under the well-balanced condition by the shaking table. However, this made the reaction force bar longer. After the initial experiments, we realized that the apparatus does not have to be at the center of the table because the shaking table has to support only the horizontal force. The vertical force is merely the gravitational force of the apparatus, which is negligible.
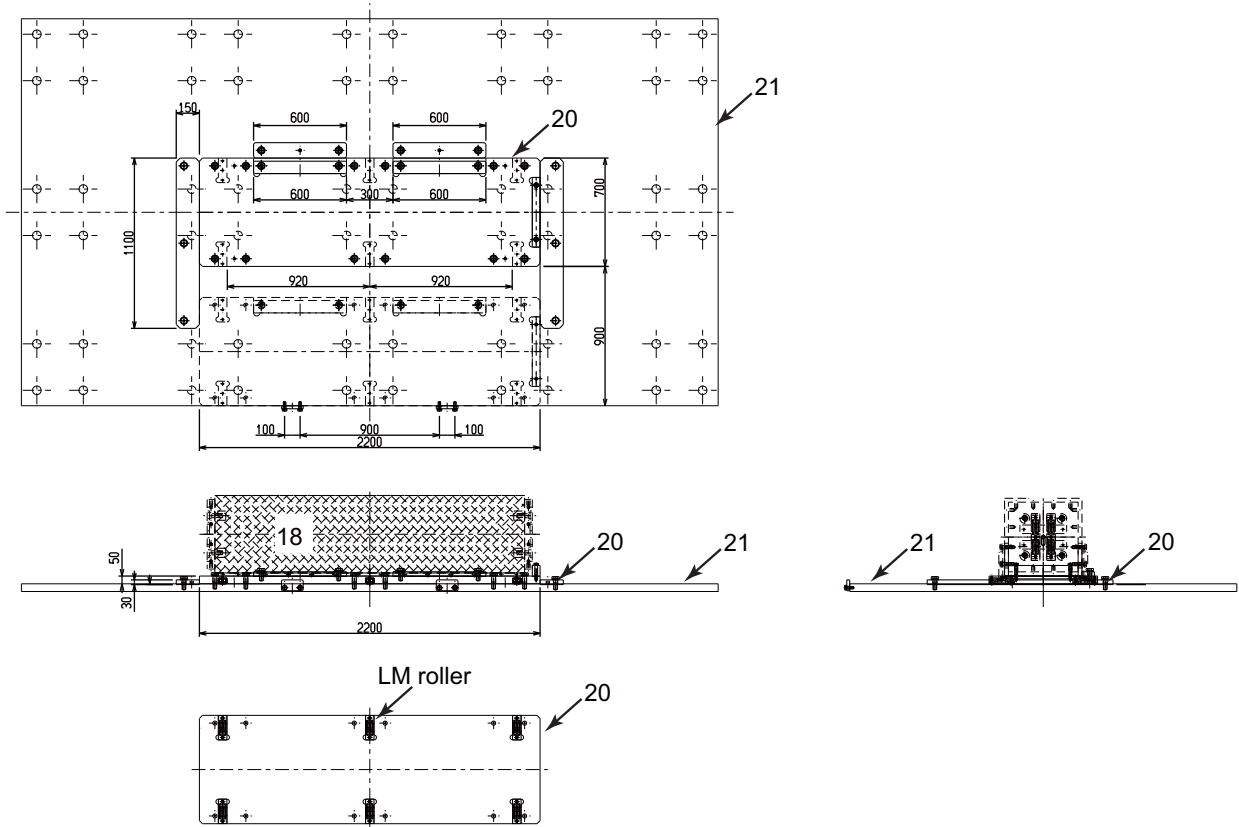
Fig. 4 Sample management unit. A sliding table was installed on the base plate to insert and extract the rock specimens before and after the experiment.
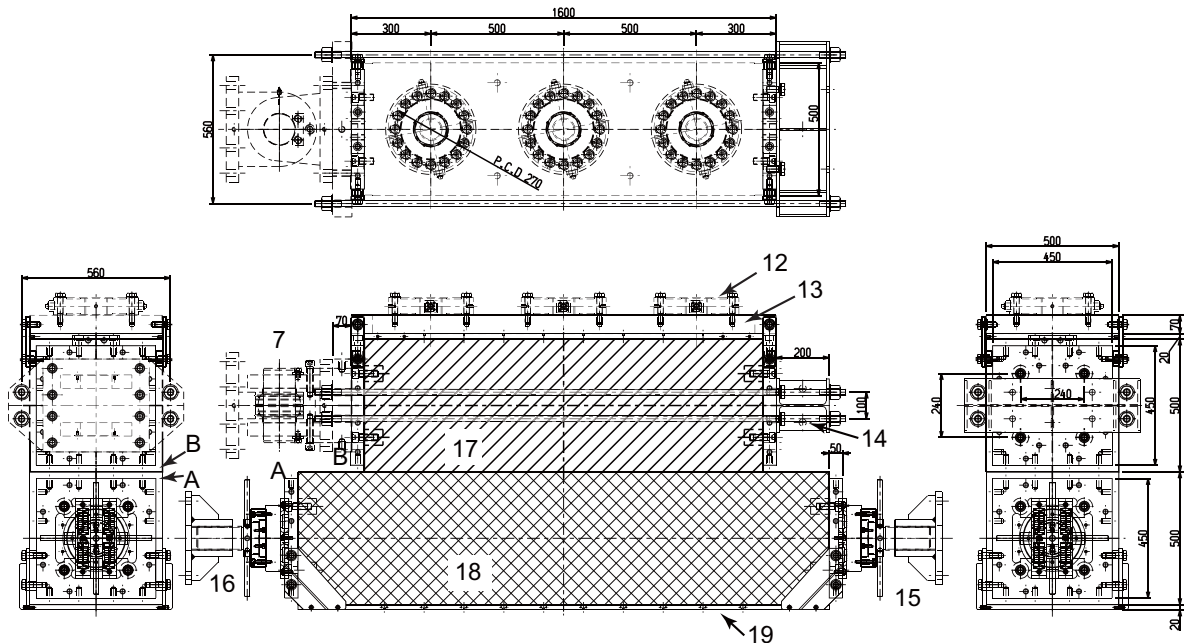
Fig. 5 Sample configuration. Beneath the lower specimen (**18**), there is a 20-mm-thick steel plate (**19**) which is used to install sensors using the holes on it. At both ends of the specimens, a 50-mm-thick steel plate is attached. On the side plate of the lower specimen, a roller system is attached to reduce the friction for vertical motion. The plates for the upper specimens are used to connect the reaction force bar as well as the PC steel bars (**14**). Above the upper specimen, a 20-mm-thick steel plate is placed for the sensor installation. Above the plate, a 70-mm-thick steel plate (**13**) is placed on which three load cells (**12**) are installed. A and B indicate the locations of laser displacement transducers (LDT and LDT-L) and their corresponding targets, respectively.
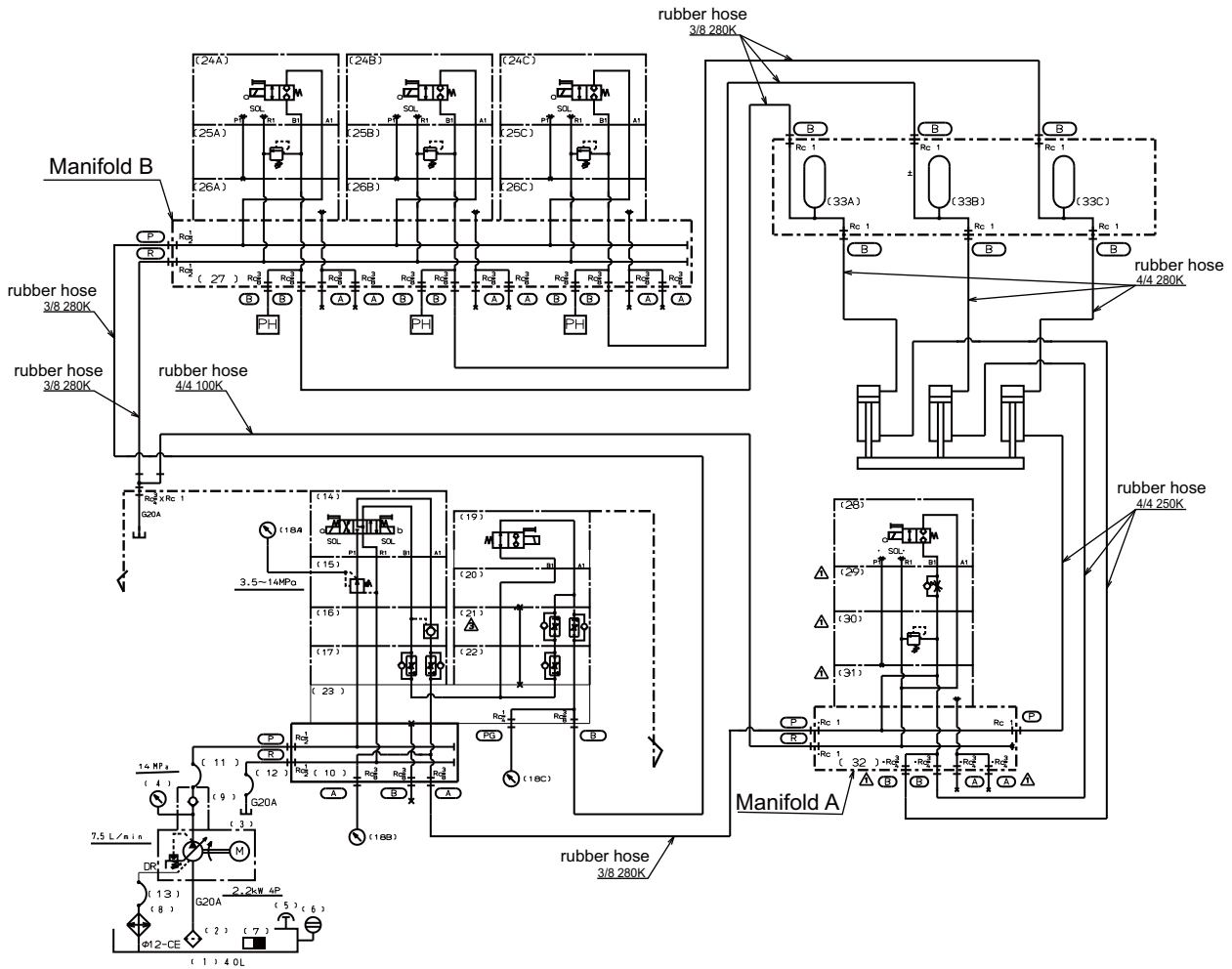
Fig. 6 Oil circuit system. The oil pressure of each actuator can be set at different levels. Each actuator has an accumulator to homogenize the pressure during the experiments. The numerals in brackets correspond to the following parts. **1:** oil tank, **2:** strainer, **3:** pump, **4**, **18:** pressure gauge (GV50-323-25M-TM), **5:** air breather, **6:** oil level gauge, **7:** magnetic separator, **8:** radiator, **9:** check valve, **10**, **27**, **32:** manifold, **11**, **12**, **13:** rubber hose, **14:** solenoid operated directional control valve, **15:** pressure reducing valve, **16:** pilot operated check valve, **17**, **29:** throttle valve, **19**, **24**, **28:** solenoid operated stop valve, **20**, **23**, **26**, **31:** spacer, **21**, **22:** pressure compensated flow control valve, **25**, **30:** relief valve, **33:** accumulator.

2.6. Sensors and Data Acquisition System

We measured the relative motion of the two rock specimens by laser displacement transducers and we measured the applied force to the specimens by load cells. For the local measurements, we used strain gauge, accelerometers, and piezoelectric sensors. The layout of the recording system is shown in **Fig. 8**. All data are acquired digitally by a combination of several data recorders synchronized by a single clock and trigger source.

The total normal force was measured by three strain gauge-type load cells (12, LC-N in **Table 1**) attached below the actuators. Three pressure gauges (PrG in **Table 1**) were attached to the oil circuit close to the actuators that provide the supplementary information on the applied normal force. The total shear force was measured by a strain gauge-type load cell (6, LC-S in **Table 1**) attached between the reaction force bar (5) and the swivel (7) that was connected to the

upper specimen. The relative displacements between the specimens were directly measured by three laser displacement transducers (LDT and LDT-L in **Table 1**). Two LDTs were used to measure the relative motion perpendicular to the shaking table motion, and an LDT-L measured the relative displacement along the shaking table motion. The two LDTs and LDT-L are attached to the upper surface of the side plate of lower specimen (A in **Fig. 5**) and their targets are on the lower surface of the side plate of upper specimen (B in **Fig. 5**).

An array of either metal strain gauges or semi-conductor two-component strain gauges (ST-S in **Table 1**) was used to monitor the shear deformation of the rock sample near the slip surface. Strain gauges were glued 20 mm off the sliding surface on the side of the rock sample at a horizontal spacing of 7.5 mm. In addition to the shear strain, normal strain was monitored using an array of one-component strain gauge (ST-N in **Table 1**).
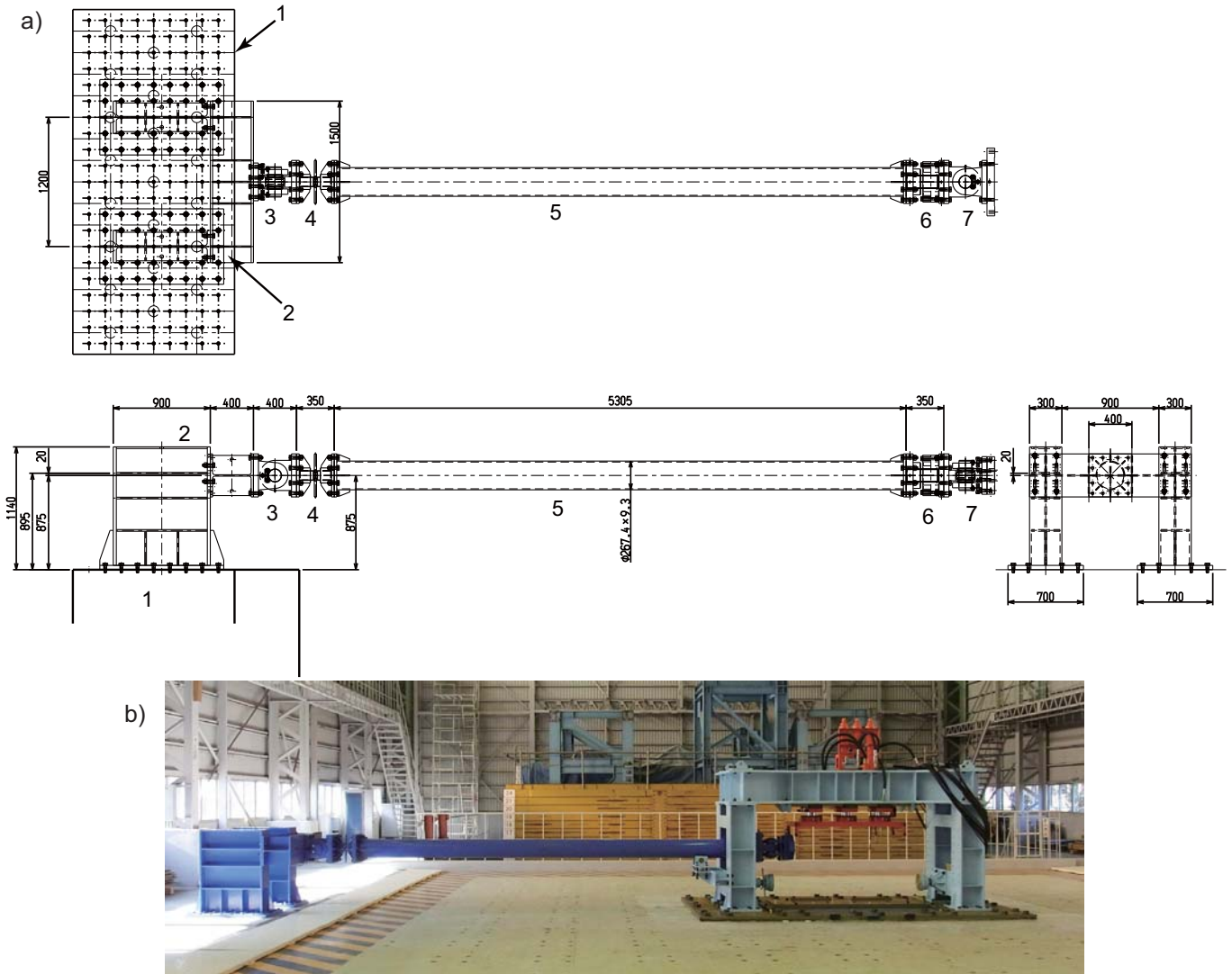
Fig. 7 Reaction force support system. To produce a dislocation between the upper and lower rock samples, the upper sample should be fixed with respect to the ground. Thus a counterforce of the shaking table should be supported outside the shaking table.

Two types of piezoelectric transducers were used. One was put on the sidewall of the sample 10 mm off the sliding surface to observe the high-frequency acoustic signals (PZT in **Table 1**). In addition to these PZTs, broadband PZTs (PZT-B in **Table 1**) were installed at the bottom of the rock specimen parallel to the slip surface. The PZT-Bs were used as receivers for the active monitoring of the signals emitted at the top of the rock specimen to measure the transmission coefficient of high-frequency waves across the sliding surface.

Four sets of three-component accelerometers (ACC in **Table 1**) were used; their resonance frequency was 50 kHz and the observation frequency range was between 100 Hz and 20 kHz.

To avoid possible data loss, we delicately recorded the output of one horizontal load cell (for shear force measurement) and three vertical load cells (for normal force measurement), three pressure gauges, a laser displacement meter, and strain gauges for the measurements of the rock specimen deformation near the sliding surfaces.

The timing of all recording systems was synchronized by the trigger pulse and a 10-MHz clock pulse generated by the triggering system (M2i.ClkDist-10M1, Spectrum, Grosshansdorf, Germany). Despite the use of this synchronizing technique, the recording unit (LX-120, TEAC, Tokyo, Japan) failed to synchronize the data acquisition timing (~3 ms difference) due to its inappropriate triggering system, which was not clearly documented in the specification sheet. The recording systems are summarized in **Table 2**.
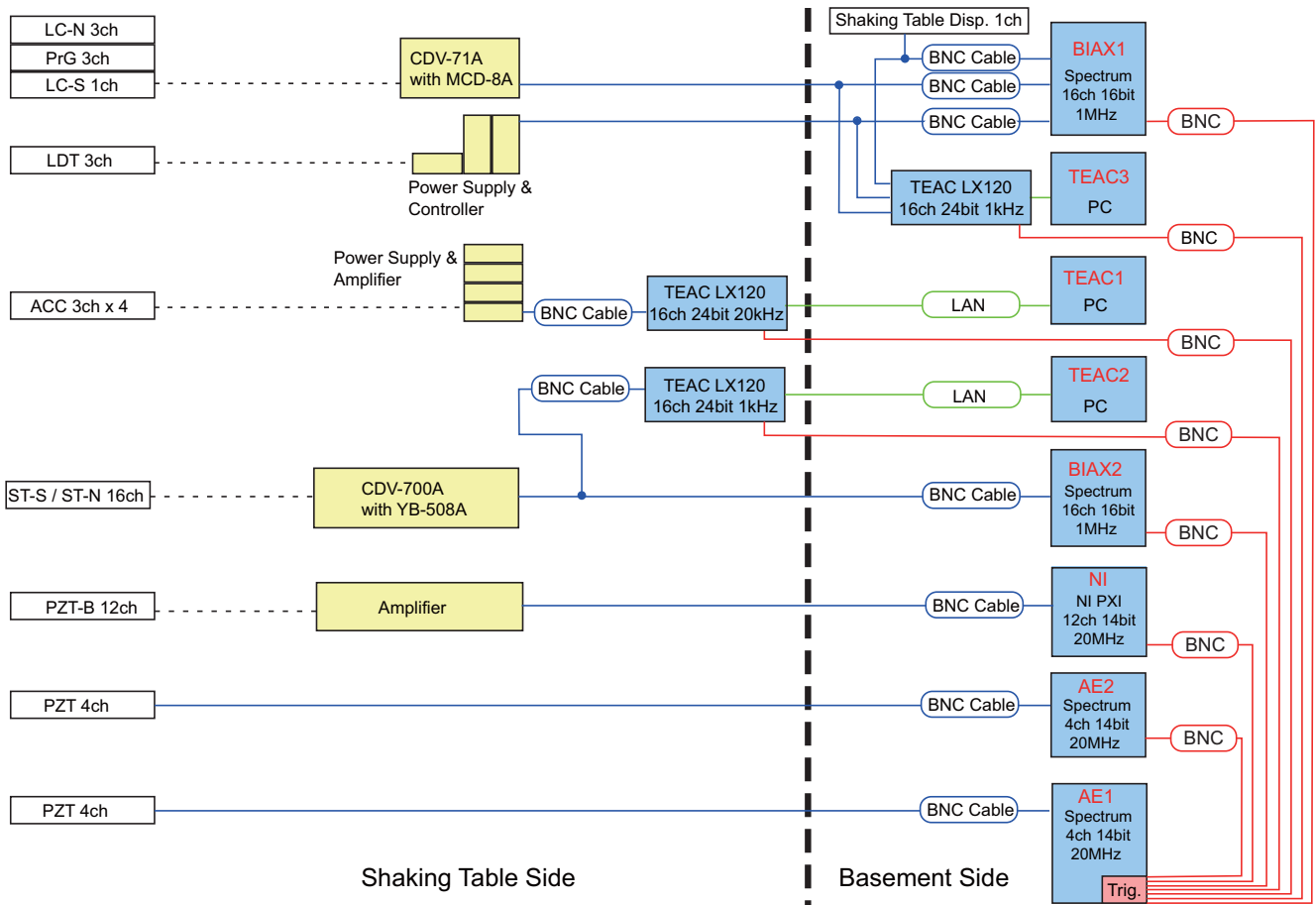
Fig. 8 Configuration of the data recording systems. Detailed information for each system can be found in **Table 2**. Red acronym in the blue box indicates the name of the recording system shown in **Table 2**.

Table 1 List of sensors.

Abbrivation	Item	Type	Specifications / Manufacturer
ST-S	Strain gouge (shear strain)	Semi-conductor , bi-axis	KSN-2-120-F3-11 / Kyowa Co. Ltd.
ST-N	Strain gouge (normal strain)	Semi-conductor, uni-axis	KSN-2-120-E4-11 / Kyowa Co. Ltd.
PZT	Piezoelectric transducer	0.5MHz, vertical	2M3D-LXY(C-6) / Fuji Ceramics Co. Ltd.
PZT-B	Piezoelectric transducer (broadband)	broadband, pre-amplified, vertical	5145SMA-1152 / Fuji Ceramics Co. Ltd.
ACC	Accerelometer	20kHz, tri-axis	SA11ZSC-TI / Fuji Ceramics Co. Ltd.
LC-S	Loadcell(shear stress)	1.2MN max, 0.05%RO	LUK-120TBSC40 / Kyowa Co. Ltd.
LC-N	Loadcell (normal stress)	400kN max, 0.1%RO	TORD-S-400KN / Tomoe Co. Ltd.
PrG	Pressure gauge	20MPa max, 0.2%RO	PGM-200KE / Kyowa Co. Ltd.
LDT	Laser displacement transducer	150mm±40mm, 0.01%RO (anti-plane&vert)	LK-G150 / Keyence Co. Ltd.
LDT-L	Long range laser displacement transducer	500mm-250mm+500mm, 0.01%RO (in-plane.)	LK-G500 / Keyence Co. Ltd.

Table 2 List of data acquisition system.

System name	Recording Device	n. of channel	Sampling rate	Resolution	Acquisition mode	Input data*
BIAX1	Spectrum M2i4741-mgt	16	1MHz	16bit	continuous	LC-S, LC-N, PrG, LDT, LDT-L
BIAX2	Spectrum M2i4741-mgt	16	1MHz	16bit	continuous	ST-S, ST-N
TEAC1	TEAC LX120	16	20kHz	24bit	continuous	ACC
TEAC2	TEAC LX120	16	1kHz	24bit	continuous	ST-S, ST-N
TEAC3	TEAC LX120	16	1kHz	24bit	continuous	LC-S, LC-N, PrG, LDT, LDT-L
AE1	Spectrum M2i4032	4	20MHz	14bit	continuous	PZT
AE2	Spectrum M2i4032	4	20MHz	14bit	continuous	PZT
NI	NI PXIe-5122	12	20MHz	14bit	continuous	PZT-B

* Acroniums are shown in **Table 1**

Table 3 List of Experimental Conditions.

Exp ID	Date	Outline	Purpose	Target velocity(mm/s)	Target displacement (mm)	Target load (kN) 1	2	3	Accumulator Pressure (MPa) 1	2	3	Gouge collection after experiment
LB01-002	2012.02.29	0mm/s, 0mm, 50t(Uniform)	Pressure Sheet Test	0	0	167	167	167				
LB01-003	2012.02.29	0mm/s, 0mm, 100t(Uniform)	Pressure Sheet Test	0	0	333	333	333				
LB01-004	2012.02.29	0mm/s, 0mm, 100t(Irregular)	Pressure Sheet Test	0	0	333	295	333				
LB01-005	2012.02.29	0mm/s, 0mm, 100t(Irregular)	Pressure Sheet Test	0	0	333	295	333				
LB01-006	2012.02.29	0mm/s, 0mm, 100t(Irregular)	Pressure Sheet Test	0	0	333	295	333				
LB01-007	2012.02.29	0mm/s, 0mm, 100t(Irregular)	Pressure Sheet Test	0	0	295	295	295				
LB01-014	2012.03.02	1mm/s, 400mm, 50t(Uniform)	Normal Exp.	1	400	167	167	167	5.9	5.9	5.9	Yes
LB01-015	2012.03.05	1mm/s, 400mm, 100t(Uniform)	Normal Exp.	1	400	333	333	333	12.0	12.0	12.0	Yes
LB01-016	2012.03.05	10mm/s, 400mm, 50t(Uniform)	Normal Exp.	10	400	167	167	167	5.9	5.9	5.9	Yes
LB01-017	2012.03.07	10mm/s, 400mm, 100t(Uniform)	Normal Exp.	10	400	333	333	333	12.0	12.0	12.0	Yes
LB01-019	2012.03.14	10mm/s, 400mm, 50t(Uniform)	Normal Exp.	10	400	167	167	167	5.9	5.9	5.9	Yes
LB01-020	2012.03.15	100mm/s, 400mm, 50t(Uniform)	Normal Exp.	100	400	333	333	333	12.0	12.0	12.0	Yes
LB01-021	2012.03.16	100mm/s, 400mm, 100t(Uniform)	Normal Exp.	100	400	167	167	167				Yes
LB01-022	2012.03.16	1000mm/s(Yoffe), 400mm, 50t(Uniform)	Normal Exp.	1000(yoffe Dc200mm)	400	333	333	333				Yes
LB01-023	2012.03.21	1000mm/s(Yoffe), 400mm, 100t(Uniform)	Normal Exp.	1000(yoffe Dc200mm)	400	333	333	333				Yes
LB01-024	2012.03.22	10mm/s, 400mm, 100t(Hetero)	Normal Exp.	10	400	333	333	250	12.0	12.0	9.0	No
LB01-025	2012.03.22	10mm/s, 400mm, 100t(Hetero)	Normal Exp.	10	400	333	333	167	12.0	12.0	5.9	No
LB01-026	2012.03.23	100mm/s, 400mm, 100t(Hetero)	Normal Exp.	100	400	333	333	167	12.0	12.0	5.9	No
LB01-027	2012.03.23	100mm/s, 400mm, 100t(Hetero)	Normal Exp.	100	400	333	333	167	12.0	12.0	5.9	No
LB01-028	2012.03.23	10mm/s, 400mm, 100t(Hetero)	Normal Exp.	10	400	333	333	167	12.0	12.0	5.9	No
LB01-029	2012.03.23	10mm/s, 400mm, 100t(Hetero)	Normal Exp.	10	400	333	333	167	12.0	12.0	5.9	No
LB01-030	2012.03.26	10mm/s, 400mm, 100t(Hetero)	Normal Exp.	10	400	350	333	167	12.0	12.0	5.9	No
LB01-031	2012.03.27	0.05Hz Triangle, 5mmpp→10mmpp, 100t(Uniform)	Stiffness Check	triangular waves, 0.05Hz	±2.5→±5	333	333	333	12.0	11.5	11.5	No
LB01-032	2012.03.27	0.05Hz Triangle, 5mmpp→10mmpp, 100t(Uniform)	Stiffness Check	triangular waves, 0.05Hz	±2.5→±5	333	333	333	12.0	11.5	11.5	No
LB01-033	2012.03.27	0.05Hz Triangle, 5mmpp→10mmpp, 100t(Uniform)	Stiffness Check	triangular waves, 0.05Hz	±2.5→±5	333	333	333	12.0	11.5	11.5	No
LB01-034	2012.03.27	0.05Hz Triangle, 5mmpp→10mmpp, 100t(Uniform)	Stiffness Check	triangular waves, 0.05Hz	±2.5→±5	333	333	333	12.0	11.5	11.5	No
LB01-035	2012.03.27	0.05Hz Triangle, 5mmpp→10mmpp, 100t(Uniform)	Stiffness Check	triangular waves, 0.05Hz	±2.5→±5	333	333	333	12.0	11.5	11.5	No
LB01-036	2012.03.27	0.05Hz Triangle, 5mmpp→10mmpp, 100t(Uniform)	Stiffness Check	triangular waves, 0.05Hz	±2.5→±5	333	333	333	12.0	11.5	11.5	No
LB01-037	2012.03.27	0.05Hz Triangle, 5mmpp→10mmpp, 100t(Uniform)	Stiffness Check	triangular waves, 0.05Hz	±2.5→±5	333	333	333	12.0	11.5	11.5	No
LB01-038	2012.03.28	0.05Hz Triangle, 5mmpp→10mmpp, 100t(Uniform)	Stiffness Check	triangular waves, 0.05Hz	±2.5→±5	333	333	333	12.0	11.5	11.5	No
LB01-039	2012.03.28	0.05Hz Triangle, 5mmpp→10mmpp, 100t(Uniform)	Stiffness Check	triangular waves, 0.05Hz	±2.5→±5	333	333	333	12.0	11.5	11.5	No
LB01-040	2012.03.28	0.1mm/s, 40mm, 100t(Uniform)	Normal Exp.	0.1	40	333	333	333	12.0	11.5	11.5	No
LB01-041	2012.03.28	0.1mm/s, 40mm, 100t(Uniform)	Normal Exp.	0.1	40	333	333	333	12.0	11.5	11.5	No
LB01-042	2012.03.28	-0.1mm/s, 40mm, 100t(Uniform)	Normal Exp.	-0.1	-40	333	333	333	12.0	11.5	11.5	No
LB01-043	2012.03.29	-0.1mm/s, 40mm, 100t(Uniform)	Normal Exp.	-0.1	-40	333	333	333	12.0	11.5	11.5	No
LB01-044	2012.03.29	0.025mm/s, 25mm, 100t(uniform)	Normal Exp.	0.025	20	333	333	333	12.0	11.5	11.5	No
LB01-045	2012.03.29	-0.025mm/s, 25mm, 100t(uniform)	Normal Exp.	-0.025	-20	333	333	333	12.0	11.5	11.5	No
LB01-046	2012.04.03	0.05Hz Triangle, 5mmpp→10mmpp, 100t(Uniform)	Stiffness Check	triangular waves, 0.05Hz	±2.5→±5	333	333	333	12.0	11.5	11.5	No
LB01-047	2012.04.03	10mm/s, 400mm, 10t(Uniform)	Normal Exp.	10	400	33.3	33.3	33.3	1.1	1.1	1.1	No
LB01-048	2012.04.03	10mm/s, 400mm, 10t(Uniform)	Normal Exp.	10	400	33.3	33.3	33.3	1.1	1.1	1.1	small pieces only
LB01-049	2012.04.03	10mm/s, 400mm, 25t(Uniform)	Normal Exp.	10	400	83.3	83.3	83.3	2.75	2.75	2.75	small pieces only
LB01-050	2012.04.04	1mm/s, 400mm, 25t(Uniform)	Normal Exp.	1	400	83.3	83.3	83.3	2.75	2.75	2.75	overflowed gouge only
LB01-051	2012.04.04	100mm/s, 400mm, 25t(Uniform)	Normal Exp.	100	400	83.3	83.3	83.3	2.75	2.75	1.1	No
LB01-052	2012.04.04	100mm/s, 400mm, 25t(Hetero)	Normal Exp.	100	400	83.3	83.3	83.3	2.75	2.75	1.1	No
LB01-053	2012.04.04	1mm/s, 400mm, 10t(Uniform)	Normal Exp.	1	400	33.3	33.3	33.3	1.1	1.1	1.1	No
LB01-054	2012.04.04	1mm/s, 400mm, 10t(Uniform)	Normal Exp.	1	400	33.3	33.3	33.3	1.1	1.1	1.1	No
LB01-055	2012.04.09	0.05Hz Triangle, 5mmpp→10mmpp, 100t(Uniform)	Stiffness Check	triangular waves, 0.05Hz	±2.5→±5	333	333	333	12	12	11.8	No
LB01-056	2012.04.09	0mm/s, 0mm, 100t(Uniform)	Sensor Test	0	0	333	333	333	12	12	11.8	No
LB01-057	2012.04.09	0.1mm/s, 40mm, 100t(Uniform)	Normal Exp.	0.1	40	333	333	333	12	12	11.8	No
LB01-058	2012.04.09	-0.1mm/s, 40mm, 100t(Uniform)	Normal Exp.	-0.1	-40	333	333	333	12	12	11.8	No
LB01-059	2012.04.09	0.1mm/s, 40mm, 100t(Uniform)	Normal Exp.	0.1	40	333	333	333	12	12	11.8	No
LB01-060	2012.04.09	-0.1mm/s, 40mm, 100t(Uniform)	Normal Exp.	-0.1	-40	333	333	333	12	12	11.8	No
LB01-061	2012.04.09	0.012Hz Triangle, 400mmpp, 25t(Uniform), ~1800s	Surface Grinding	triangular waves, 0.012Hz	±200	83.3	83.3	83.3	2.75	2.75	2.75	No
LB01-062	2012.04.10	0mm/s, 0mm, 25t(Uniform)	Sensor Test	0	0	83.3	83.3	83.3	2.75	2.75	2.75	No
LB01-063	2012.04.10	100mm/s, 400mm, 25t(Uniform)	Normal Exp.	100	400	83.3	83.3	83.3	2.75	2.75	2.75	No
LB01-064	2012.04.10	0.012Hz Triangle, 400mmpp, 50t(Uniform), ~600s	Surface Grinding	triangular waves, 0.012Hz	±200	167	167	167	6	6	6	No
LB01-065	2012.04.10	0.012Hz Triangle, 400mmpp, 25t(Uniform), ~1800s	Surface Grinding	triangular waves, 0.012Hz	±200	83.3	83.3	83.3	2.75	2.75	2.75	No
LB01-066	2012.04.10	0mm/s, 0mm, 25t(Uniform)	Sensor Test	0	0	83.3	83.3	83.3	2.75	2.75	2.75	No
LB01-067	2012.04.11	100mm/s, 400mm, 25t(Uniform)	Normal Exp.	100	400	83.3	83.3	83.3	2.75	2.75	2.75	No
LB01-068	2012.04.11	0.05Hz Triangle, 5mmpp→10mmpp, 100t(Uniform)	Stiffness Check	triangular waves, 0.05Hz	±2.5→±5→0→±2	83.3	83.3	83.3	2.75	2.75	2.75	No
LB01-069	2012.04.11	0.1mm/s, 40mm, 25t(Uniform)	Normal Exp.	0.1	40	83.3	83.3	83.3	2.75	2.75	2.75	No
LB01-070	2012.04.11	-0.1mm/s, 40mm, 25t(Uniform)	Normal Exp.	-0.1	-40	83.3	83.3	83.3	2.75	2.75	2.75	No
LB01-071	2012.04.11	1mm/s, 400mm, 25t(Uniform)	Normal Exp.	1	400	83.3	83.3	83.3	2.75	2.75	2.75	No
LB01-072	2012.04.11	10mm/s, 400mm, 25t(Uniform)	Normal Exp.	10	400	83.3	83.3	83.3	2.75	2.75	2.75	No
LB01-073	2012.04.11	100mm/s, 400mm, 25t(Uniform)	Normal Exp.	100	400	83.3	83.3	83.3	2.75	2.75	2.75	No
LB01-074	2012.04.11	30mm/s, 400mm, 25t(Uniform)	Normal Exp.	30	400	83.3	83.3	83.3	2.75	2.75	2.75	Yes
LB01-075	2012.04.12	0.012Hz Triangle, 400mmpp, 25t(Uniform), ~1800s	Surface Grinding	triangular waves, 0.012Hz	±200	83.3	83.3	83.3	2.75	2.75	2.75	No
LB01-076	2012.04.12	10mm/s, 400mm, 25t(Uniform)	Normal Exp.	10	400	83.3	83.3	83.3	2.75	2.75	2.75	No
LB01-077	2012.04.12	100mm/s, 400mm, 25t(Uniform)	Normal Exp.	100	400	83.3	83.3	83.3	2.75	2.75	2.75	No
LB01-078	2012.04.12	10mm/s, 400mm, 50t(Uniform)	Normal Exp.	10	400	167	167	167	6	6	6	No
LB01-079	2012.04.22	0mm/s, 0mm, 50t(Uniform)	Sensor Test	0	0	167	167	167	6	6	6	No

ID	Date	Loading conditions	Category	Control	Amplitude	(1)	(2)	(3)	(4)	(5)	(6)	Notes
LB01-080	2012.04.22	10mm/s, 400mm, 50t(Uniform)	Normal Exp.	10	400	167	167	167	167	6	6	No
LB01-081	2012.04.22	10mm/s, 400mm, 50t(Uniform)	Normal Exp.	10	400	167	167	167	167	6	6	No
LB01-082	2012.04.22	10mm/s, 400mm, 50t(Uniform)	Normal Exp.	10	400	167	167	167	167	6	6	No
LB01-083	2012.04.24	0.05Hz Sine, 400mmpp, 0t	Sensor Test	sine waves, 0.05Hz	±100	0	0	0	0	6	6	No
LB01-084	2012.04.24	1mm/s, 400mm, 0t	Sensor Test	1	400	0	0	0	0	6	6	No
LB01-085	2012.04.24	100mm/s, 400mm, 0t	Sensor Test	100	400	0	0	0	0	6	6	No
LB01-086	2012.04.25	0.05HzTriangle, 2mmpp→4mmpp, 50t(Uniform)	Stiffness Check	triangular waves, 0.1Hz	±1→±2	167	167	167	167	6	6	No
LB01-087	2012.04.25	0.1mm/s, 40mm, 50t(Uniform)	Normal Exp.	0.1	-40	167	167	167	167	6	6	No
LB01-088	2012.04.25	-0.1mm/s, 40mm, 50t(Uniform)	Normal Exp.	-0.1	400	167	167	167	167	6	6	No
LB01-089	2012.04.25	100mm/s, 400mm, 50t(Uniform)	Normal Exp.	100	400	167	167	167	167	6	6	No
LB01-090	2012.04.26	0.1mm/s, 40mm, 50t(Uniform)	Normal Exp.	0.1	40	167	167	167	167	6	6	No
LB01-091	2012.04.26	0.1mm/s, 40mm, 50t(Uniform)	Normal Exp.	0.1	-40	167	167	167	167	6	6	No
LB01-092	2012.04.26	0.1mm/s, 40mm, 50t(Uniform)	Normal Exp.	0.1	40	167	167	167	167	6	6	No
LB01-093	2012.04.26	-0.1mm/s, 40mm, 50t(Uniform)	Normal Exp.	-0.1	-40	167	167	167	167	6	6	No
LB01-094	2012.04.26	1mm/s, 400mm, 50t(Uniform)	Normal Exp.	1	400	167	167	167	167	6	6	No
LB01-095	2012.04.26	10mm/s, 400mm, 50t(Uniform)	Normal Exp.	10	400	167	167	167	167	6	6	No
LB01-096	2012.04.27	0.1mm/s, 40mm, 100t(Uniform)	Normal Exp.	0.1	40	333	333	333	333	12	12	No
LB01-097	2012.04.27	-0.1mm/s, 40mm, 100t(Uniform)	Normal Exp.	-0.1	-40	333	333	333	333	12	12	No
LB01-098	2012.04.27	0.05HzTriangle, 5mmpp→10mmpp, 100t(Uniform)	Stiffness Check	triangular waves, 0.05Hz	±2.5→±5	333	333	333	333	12	12	small pieces only
LB01-099	2012.04.27	1mm/s, 400mm, 100t(Uniform)	Normal Exp.	1	400	333	333	333	333	12	12	small pieces only
LB01-100	2012.04.27	10mm/s, 400mm, 100t(Uniform)	Normal Exp.	10	400	333	333	333	333	12	12	small pieces only
LB01-101	2012.04.27	0mm/s, 0mm, 100t(Uniform)	Sensor Test	0	0	333	333	333	333	12	12	Yes
LB01-102	2012.04.27	0mm/s, 0mm, 100t(Uniform)	Sensor Test	0	0	333	333	333	333	12	12	No
LB01-103	2012.05.07	0.05HzTriangle, 5mmpp→10mmpp, 100t(Uniform)	Stiffness Check	triangular waves, 0.05Hz	±2.5→±5	333	333	333	333	12	12	No
LB01-104	2012.05.07	0.1mm/s, 40mm, 100t(Uniform)	Normal Exp.	0.1	40	333	333	333	333	12	12	No
LB01-105	2012.05.07	0.05HzTriangle, 5mmpp→10mmpp, 100t(Uniform)	Stiffness Check	triangular waves, 0.05Hz	±2.5→±5	333	333	333	333	12	12	No
LB01-106	2012.05.07	0.1mm/s, 40mm, 100t(Uniform)	Normal Exp.	0.1	40	333	333	333	333	12	12	No
LB01-107	2012.05.07	0.05HzTriangle, 5mmpp→10mmpp, 100t(Uniform)	Stiffness Check	triangular waves, 0.05Hz	±2.5→±5	333	333	333	333	12	12	No
LB01-108	2012.05.07	0.1mm/s, 40mm, 100t(Uniform)	Normal Exp.	0.1	40	333	333	333	333	12	12	No
LB01-109	2012.05.07	0.05HzTriangle, 5mmpp→10mmpp, 100t(Uniform)	Stiffness Check	triangular waves, 0.05Hz	±2.5→±5	333	333	333	333	12	12	No
LB01-110	2012.05.08	0.05HzTriangle, 5mmpp→10mmpp, 100t(Uniform)	Stiffness Check	triangular waves, 0.05Hz	±2.5→±5	333	333	333	333	12	12	Yes
LB01-111	2012.05.08	0.1mm/s, 40mm, 100t(Uniform)	Normal Exp.	0.1	40	333	333	333	333	12	12	No
LB01-112	2012.05.08	0.05HzTriangle, 5mmpp→10mmpp, 100t(Uniform)	Stiffness Check	triangular waves, 0.05Hz	±2.5→±5	333	333	333	333	12	12	small pieces only
LB01-113	2012.05.08	1mm/s, 400mm, 100t(Uniform)	Normal Exp.	1	400	333	333	333	333	12	12	No
LB01-114	2012.05.08	0.05HzTriangle, 5mmpp→10mmpp, 100t(Uniform)	Stiffness Check	triangular waves, 0.05Hz	±2.5→±5	333	333	333	333	12	12	small pieces only
LB01-115	2012.05.08	1mm/s, 400mm, 100t(Uniform)	Normal Exp.	1	400	333	333	333	333	12	12	small pieces only
LB01-116	2012.05.08	0.05HzTriangle, 5mmpp→10mmpp, 100t(Uniform)	Stiffness Check	triangular waves, 0.05Hz	±2.5→±5	333	333	333	333	12	12	small pieces only
LB01-117	2012.05.08	1mm/s, 400mm, 100t(Uniform)	Normal Exp.	1	400	333	333	333	333	12	12	No
LB01-118	2012.05.14	1Hz→30Hz sweep, 0.5m/s², 0t	Sensor Test	sweep wavesm 1-30Hz	50gal	333	333	333	333	12	12	No
LB01-119	2012.05.14	0.05HzTriangle, 5mmpp→10mmpp, 100t(Uniform)	Stiffness Check	triangular waves, 0.05Hz	±2.5→±5	333	333	333	333	12	12	No
LB01-120	2012.05.14	0.1mm/s, 40mm, 100t(Uniform)	Normal Exp.	0.1	40	333	333	333	333	12	12	small pieces only
LB01-121	2012.05.14	0.1mm/s, 40mm, 100t(Uniform)	Normal Exp.	0.1	40	333	333	333	333	12	12	No
LB01-122	2012.05.14	0.1mm/s, 40mm, 100t(Uniform)	Normal Exp.	0.1	40	333	333	333	333	12	12	No
LB01-123	2012.05.15	0.05HzTriangle, 5mmpp→10mmpp, 100t(Uniform)	Stiffness Check	triangular waves, 0.05Hz	±2.5→±5	333	333	333	333	12	12	No
LB01-124	2012.05.15	0.1mm/s, 40mm, 100t(Uniform)	Normal Exp.	0.1	40	333	333	333	333	12	12	No
LB01-125	2012.05.15	0.1mm/s, 40mm, 100t(Uniform)	Normal Exp.	0.1	40	333	333	333	333	12	12	Yes
LB01-126	2012.05.16	0.05HzTriangle, 5mmpp→10mmpp, 100t(Uniform)	Stiffness Check	triangular waves, 0.05Hz	±2.5→±5	333	333	333	333	12	12	No
LB01-127	2012.05.16	0.1mm/s, 40mm, 100t(Uniform)	Normal Exp.	0.1	40	333	333	333	333	12	12	No
LB01-128	2012.05.16	0.1mm/s, 40mm, 100t(Uniform)	Normal Exp.	0.1	40	333	333	333	333	12	12	No
LB01-129	2012.05.16	0.05HzTriangle, 5mmpp→10mmpp, 100t(Uniform)	Stiffness Check	triangular waves, 0.05Hz	±2.5→±5	333	333	333	333	12	12	No
LB01-130	2012.05.16	0.1mm/s, 40mm, 100t(Uniform)	Stiffness Check	triangular waves, 0.05Hz	40	333	333	333	333	12	12	No
LB01-131	2012.05.17	0mm/s, 0mm, 100t(Uniform)	Stiffness Check	0	0	333	333	333	333	12	12	No
LB01-132	2012.05.17	0.1mm/s, 40mm, 100t(Uniform)	Normal Exp.	0.1	40	333	333	333	333	12	12	No
LB01-133	2012.05.17	0.05HzTriangle, 5mmpp→10mmpp, 100t(Uniform)	Stiffness Check	triangular waves, 0.05Hz	±2.5→±5	333	333	333	333	12	12	No
LB01-134	2012.05.17	0.1mm/s, 40mm, 100t(Uniform)	Normal Exp.	0.1	40	333	333	333	333	12	12	No
LB01-135	2012.05.17	-0.1mm/s, 40mm, 100t(Uniform)	Normal Exp.	-0.1	-40	333	333	333	333	12	12	No
LB01-136	2012.05.17	0.05HzTriangle, 5mmpp→10mmpp, 100t(Uniform)	Stiffness Check	triangular waves, 0.05Hz	±2.5→±5	333	333	333	333	12	12	No
LB01-137	2012.05.17	0.05HzTriangle, 5mmpp→10mmpp, 100t(Hetero)	Stiffness Check	triangular waves, 0.05Hz	±2.5→±5	333	333	333	333	12	12	No
LB01-138	2012.05.17	0.1mm/s, 40mm, 100t(Hetero)	Normal Exp.	0.1	40	167	167	167	167	6	6	No
LB01-139	2012.05.17	0.1mm/s, 40mm, 100t(Hetero)	Normal Exp.	0.1	40	167	167	167	167	6	6	No
LB01-140	2012.05.18	1mm/s, 400mm, 100t(Hetero)	Normal Exp.	1	400	167	167	167	167	6	6	No
LB01-141	2012.05.18	0.1mm/s→1mm/s, 5mm→8, 100t(Hetero)	Normal Exp.	0.1mm/s→1mm/s→0.1mm/s→1mm/s	80	167	167	167	167	6	6	No
LB01-142	2012.05.18	1mm/s, 400mm, 100t(Uniform)	Normal Exp.	1	400	333	333	333	333	12	12	No
LB01-143	2012.05.18	0.05HzTriangle, 5mmpp→10mmpp, 100t(Uniform)	Stiffness Check	triangular waves, 0.05Hz	±2.5→±5	333	333	333	333	12	12	No
LB01-144	2012.05.18	0.1mm/s, 40mm, 100t(Uniform)	Normal Exp.	0.1	40	333	333	333	333	12	12	No
LB01-145	2012.05.18	0.05HzTriangle, 5mmpp→10mmpp, 100t(Uniform)	Stiffness Check	triangular waves, 0.05Hz	±2.5→±5	333	333	333	333	12	12	No
LB01-146	2012.05.18	0.1mm/s, 40mm, 100t(Hetero)	Normal Exp.	0.1	40	333	333	333	333	12	12	No
LB01-147	2012.05.23	0.05HzTriangle, 5mmpp→10mmpp, 100t(Uniform)	Stiffness Check	triangular waves, 0.05Hz	±2.5→±5	333	333	333	333	12	12	No
LB01-148	2012.05.23	0.1mm/s, 40mm, 100t(Hetero)	Normal Exp.	0.1	40	333	333	333	333	12	12	No
LB01-149	2012.05.23	10mm/s, 400mm, 100t(Uniform)	Normal Exp.	10	400	333	333	333	333	12	12	Yes

a)

LB01-003 Pressure Profile

b)
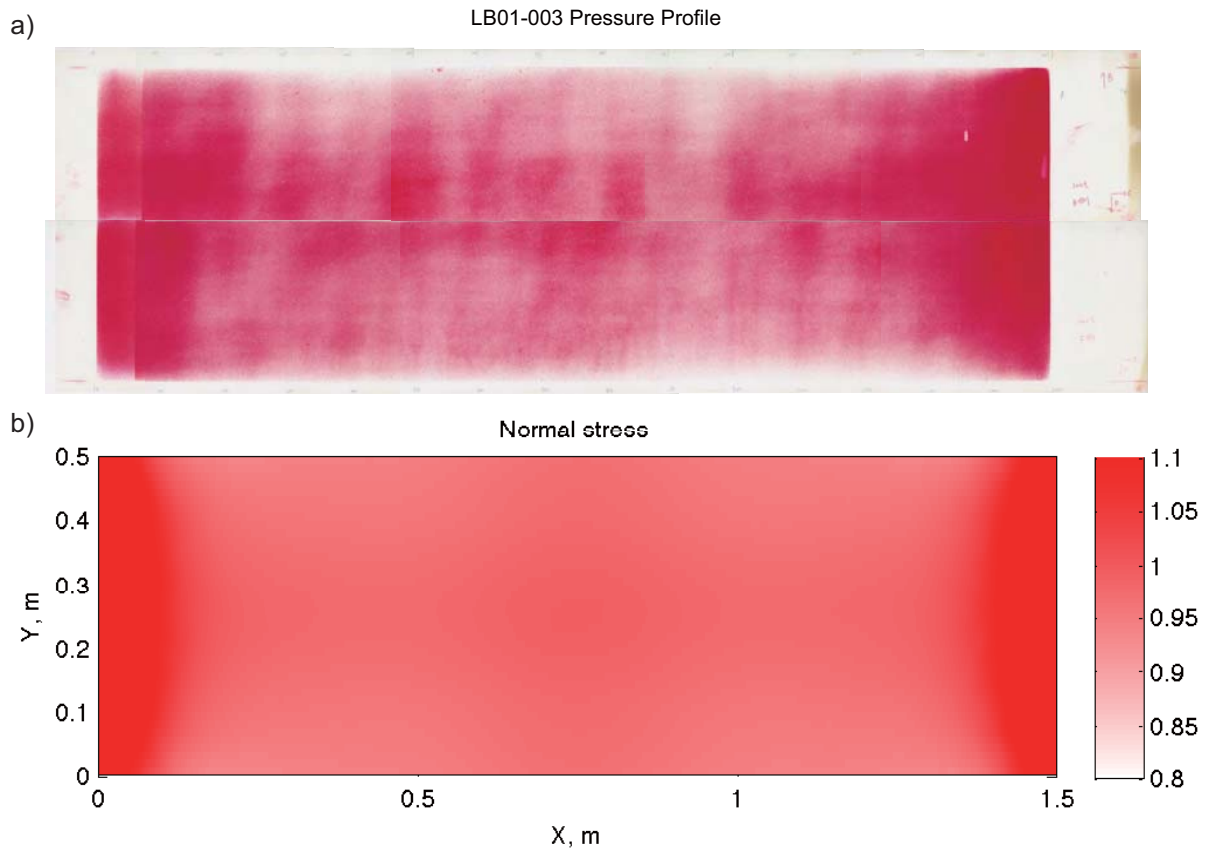
Fig. 9 **a)** Distribution of normal stress on the slip surface measured by the pressure-sensing sheet (Fujifilm Co. Ltd. PRESCALE LLW), when 0.333 MN normal force was applied by each actuator, which is expected to apply 1.3 MPa normal stress on the slip surface. **b)** Normal stress distribution computed by the finite element simulation under the same conditions as those used for the pressure-sensing sheet test.

3. Experiment Results

We have conducted about 140 experiments between 29 February 2012 and 23 May 2012 using the G-1 apparatus. The details are shown in **Table 3**.

3.1 Rock Specimen Used in the Experiments

We used gabbro from Tamil Nadu, India as rock specimens in the experiments. Young's modulus, Poisson ratio, rigidity, P- and S-wave velocities, and density of this specimens are 103 GPa, 0.31, 38 GPa, 6.92 km/s, 3.62 km/s, and 2980 kg/m^3, respectively [Sekistone Co. Ltd., 2012, personal comm.]. Major minerals included in the specimen are plagioclase, clinopyroxene, hornblende, biotite, ilmenite and hematite [Hirose and Shimamoto, 2003].

3.2 Normal Stress Distribution

First, we conducted pressure-sensing sheet experiments (from LB01-002 to LB01-007 in **Table 3**) to evaluate the uniformity of the contact conditions between the two rock specimens when the normal stress is applied to 0.66 MPa (LB01-002) and 1.3 MPa (from LB01-003 to LB01-007).

Fig. 9a shows the obtained image of the pressure-sensing sheet for the LB01-003 experiment. Since the width of the sheet was 270 mm, we had to use two sheets located in parallel for each experiment. An A3 size scanner was then

used to digitize the image. Finally, ten sets of A3 image data were connected by an image software program to obtain a single image of the pressure distribution. This is the cause of some discontinuities at the center of the image.

In this image, the depth of the red color is proportional to the pressure (dark red represents high pressure). We could not determine the absolute value of the pressure since the absolute color depends on the temperature, humidity, and contact time of the sheet, but we observed the relative distribution of the pressure applied to the slip surface.

The simulation results obtained by a finite element method (FEM) are shown in **Fig. 9b**; the initial and boundary conditions were the same as those used for the stress-sensing sheet test. We used software called Salome-Meca in which Salome is used as the pre- and post- processor and Code_Aster is used for the solver. We assume that the system is composed of either rock or steel, whose elastic constants are Young modulus of 103 GPa and Poisson ratio of 0.31 for rock and 205 GPa and 0.30 for steel. The system was divided into 362,946 tetrahedral elements whose dimension was less than 25 mm. The lower surface of the lower specimen was fixed, and normal force was applied to the jacks.

A quick glance in **Fig. 9** indicates that the computed

normal stress distribution is similar to that of the observed. However, with a closer look, some differences can be seen on a micro scale. This could be due to the material heterogeneity and/or tiny topographic differences in the surfaces of the specimens. In any case, this comparison suggests that the FEM prediction can give us a rough image of the normal stress distribution on the sliding surface.

3.3 Stiffness of the Apparatus

Using the stick-slip waveforms obtained by the experiments LB01-014 to LB01-023, Togo *et al.* [2014] estimated the stiffness of the apparatus based on the method used by Shimamoto *et al.* [1980] (originally suggested by Ohnaka [1973, 1978]). They estimated the total stiffness of the apparatus as 0.119 GN/m.

In addition, to evaluate the static stiffness of the individual elements of the apparatus, several quasi-static loading tests (LB01-031 to LB01-039 in **Table 3**) were carried out. A laser displacement transducer (Micro-Epsilon, optoNCDT ILD-1700-50) and a target are attached to both ends of the element to measure its deformation due to shear loading. Dynamic range of the transducer and its resolution were 50 mm and 3 μm, respectively. A shear load was applied by displacing the shaking table under a constant normal stress of 1.33 MPa on the simulated fault. A triangular-shaped displacement waveform with a frequency of 0.05 Hz was used as a motion of shaking table. The amplitude of the shaking table displacement was 2.5 mm for the first 5-10 cycles and increased to 5.0 mm for another 5-10 cycles. Under this condition, no obvious slip on the simulated fault was observed.

A typical example of shear force measured by the shear force gauge (6) and deformation during the loading test measured by the displacement transducer are shown in **Fig. 10a** and **b**. This example shows the deformation of the turnbuckle (4). Note that a negative value of the deformation represents shortening of the element due to compression by the shear loading. Although the shear force and the deformation were basically linear with respect to the displacement of shaking table, nonlinear distortions were observed. This nonlinear behavior is mainly caused by complex deformation (play) at connecting parts. In **Fig. 10c**, the shear force is plotted as a function of the deformation. It clearly demonstrates the effect of the play at low shear loading. The stiffness of element is estimated from the gradient of the shear force with respect to the deformation, excluding the data at the low shear forces. A red line in **Fig. 10c** represents the estimated gradient determined with the least-square method under the compressional condition. The stiffness estimated under the extensional condition (a blue line in **Fig. 10c**) is smaller than that under the compressional condition in all elements, except for the specimen fixing screw (15), which is not connected
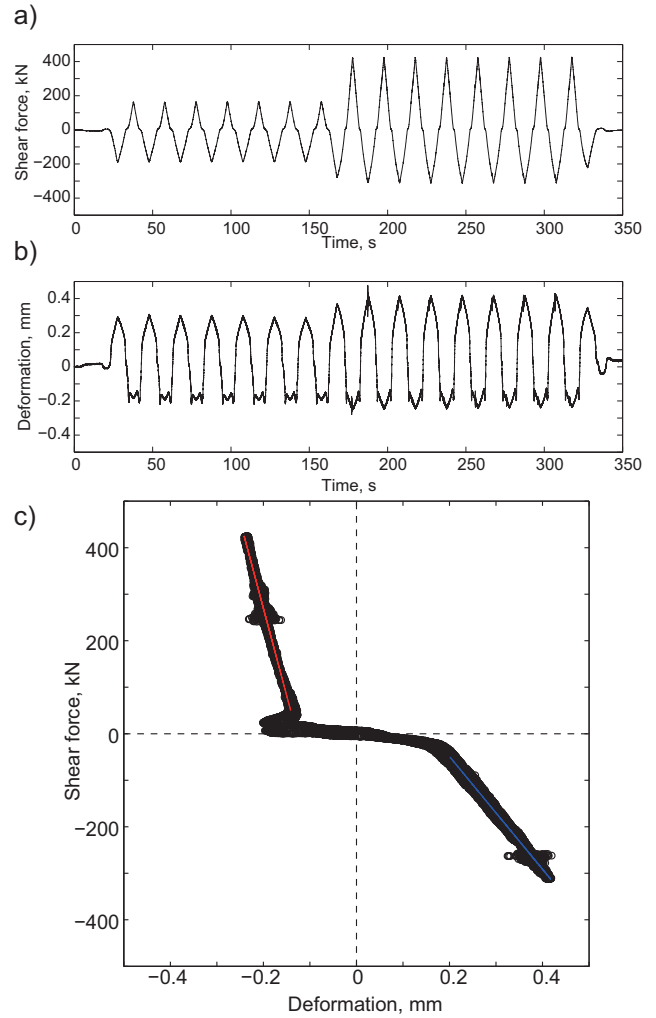
Fig. 10 a) Temporal variation of the shear force in response to the triangular displacement motion of shaking table. **b)** Temporal variation of the length change of the turnbuckle (4) due to the triangular displacement shaking table motion. **c)** Force - deformation diagram for the turnbuckle (4), whose gradients corresponds to the stiffness of the turnbuckle (4).

to the lower specimen (18) and thus should not be stretched under the extensional condition. The estimated stiffness of each element is shown in **Fig. 11**. In addition to the stiffness for each part of the apparatus, the stiffness estimated from the measurements at the western edge of shaking table as well as the sidewall of the table is shown at the bottom of **Fig. 11**. This stiffness should be equal to the stiffness of the system assuming that the deformation of the table itself is negligible. The total stiffness of this apparatus was estimated as 0.1 GN/m. This stiffness is one order of magnitude softer than the existing apparatus [e.g., Scholz *et al.*, 1968] because of the size of the apparatus. Due to this rather low stiffness, the stick-slip events occurred frequently at high velocity loading,
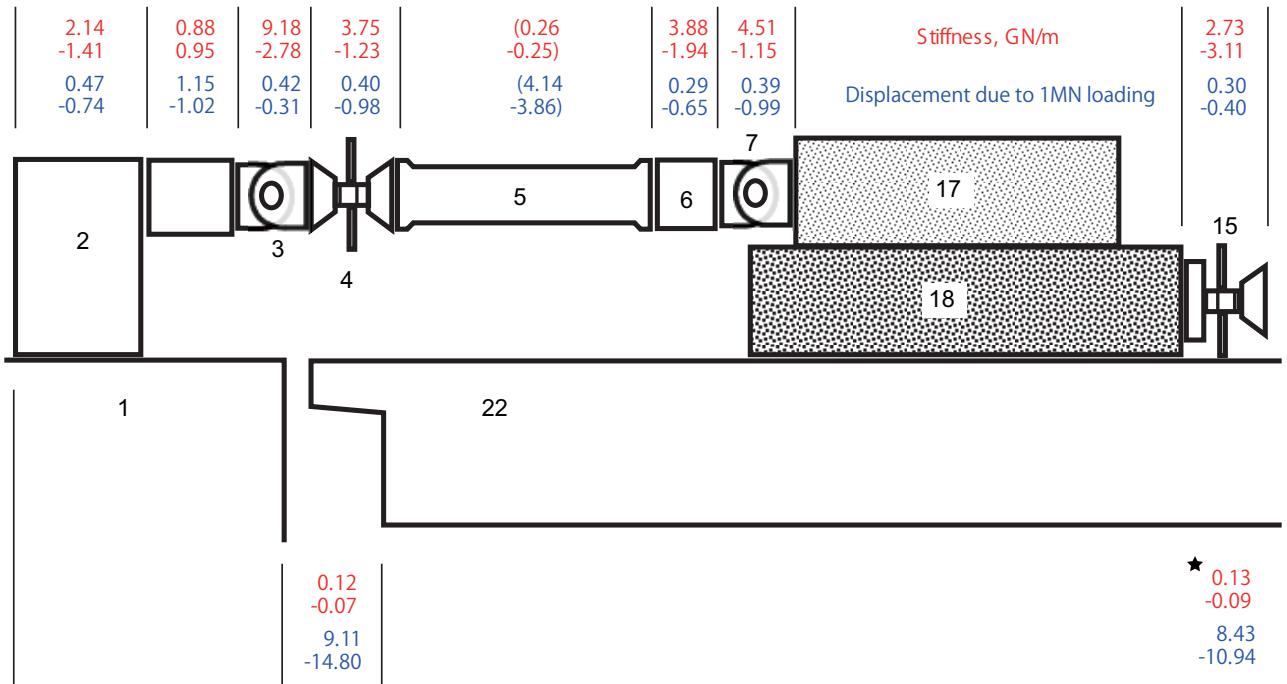
Fig. 11 Stiffness measured by the experiments (from LB01-031 to LB-039). Each value is estimated from direct measurements by the LDT except for that of the reaction force bar (5), which was extrapolated from other surrounding measurement. Red numbers indicate the stiffness values where the gradient of displacement due to the amount of applied force is measured. Blue numbers are the amount of displacements when 1 MN force is applied. Positive numbers show compressional motion, and negative numbers are for the extensional motion. The values with solid star are estimated from the displacements measured by the sensors equipped at both side of the shaking table. Numeral indexes in the figure correspond to the parts number shown in **Fig. 1**.

at which weakening of the rock material at high slip velocity took place that the apparatus could not catch up with [e.g., Dieterich, 1978a].

3.4 Macroscopic Friction Coefficient

One of the main purposes of the present study was to investigate the specimen size dependence of the friction. For the last several decades, rock friction experiments have been intensively carried out to investigate the frictional properties of rock samples under different pressures, temperatures, loading rates, and hydraulic conditions. However, in most of those experiments, the size of the rock sample was on the order of centimeters because of the physical constraints of the apparatus [see Di Toro *et al.* 2011 for an example].

We conducted several experiments under a constant loading rate with room temperature and room humidity, applying 1.33 MPa normal stress. The results are shown in **Fig. 12**, plotted with the results of small rock samples compiled by Di Toro *et al.* [2011]. In that plot, we selected the steady-state part of the data (the latter part of the experiments) and computed the mean value and standard deviations of the stress ratio measured by the horizontal and vertical load cells. We confirmed that variation of the friction in time follows the normal distribution thus the mean values and their standard deviations have statistical meanings. It should be noted that in the present experiments, the accurate slip rate could not

be measured because of the occurrence of stick slip events. Therefore, in **Fig. 12**, the friction data in this study are plotted as a function of loading rate. **Table 4** also gives the values of friction coefficient. As can be seen in the figure, the friction behavior with respect to the loading velocity is quite consistent with the results compiled by Di Toro *et al.* [2011].

We have not yet made a detailed comparison between the macroscopic friction (i.e., friction measured outside the specimen) and microscopic friction (i.e., friction measured inside the specimen), but a slight dependence of the friction on the sliding area may exist, which could be a good target for the next experiments. In the present experiments, we did not measure the normal strain parallel to the slip direction along the slipping surface because of the limited number of recording channels, which made the estimation of the normal stress difficult.

3.5 Rupture Propagation Monitoring

From the observations provided by the strain gauge array (ST-S in **Table 1**) along the slip surface (**Fig. 13**), we detected ruptures propagating along the fault, some of which did not reach the edge of the rock specimens. Hereafter we refer to these ruptures as "confined slip events" after Dieterich *et al.* [1978]. Since such events were not affected by the edge of the specimens during the propagation of the rupture, they can be considered events similar to natural earthquakes.
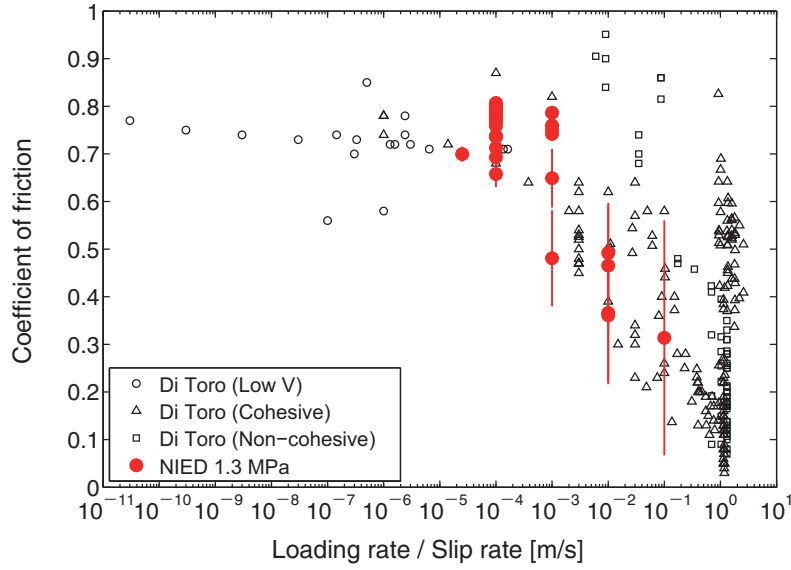
Fig. 12 Average coefficients of friction are plotted as a function of loading rate (red solid circles) with their standard deviations (red vertical bars). Open squares, triangles and circles are the values taken from Di Toro *et al.* [2011] and plotted assuming that loading rate and slip rate are equivalent.

Table 4 Coefficient of friction measured by the experiments.

Experiment ID	Loading rate [m/s]	Average coefficient of friction	Standard deviation
LB01-044	2.50E-05	0.6994	0.0157
LB01-040	1.00E-04	0.6578	0.0276
LB01-041	1.00E-04	0.6929	0.0195
LB01-057	1.00E-04	0.7375	0.0167
LB01-059	1.00E-04	0.7588	0.0130
LB01-096	1.00E-04	0.7128	0.0142
LB01-104	1.00E-04	0.7685	0.0101
LB01-106	1.00E-04	0.7809	0.0148
LB01-108	1.00E-04	0.7905	0.0146
LB01-111	1.00E-04	0.7887	0.0136
LB01-120	1.00E-04	0.7364	0.0105
LB01-121	1.00E-04	0.7367	0.0080
LB01-122	1.00E-04	0.7713	0.0049
LB01-124	1.00E-04	0.7772	0.0094
LB01-125	1.00E-04	0.8030	0.0075
LB01-127	1.00E-04	0.7724	0.0103
LB01-129	1.00E-04	0.8004	0.0080
LB01-132	1.00E-04	0.7896	0.0132
LB01-134	1.00E-04	0.8068	0.0109
LB01-144	1.00E-04	0.7813	0.0040
LB01-146	1.00E-04	0.7960	0.0014
LB01-148	1.00E-04	0.7994	0.0084
LB01-015	1.00E-03	0.4808	0.1010
LB01-099	1.00E-03	0.7419	0.0135
LB01-113	1.00E-03	0.6492	0.0618
LB01-115	1.00E-03	0.7597	0.0174
LB01-117	1.00E-03	0.7513	0.0153
LB01-142	1.00E-03	0.7865	0.0140
LB01-017	1.00E-02	0.3661	0.1444
LB01-019	1.00E-02	0.3612	0.1448
LB01-100	1.00E-02	0.4921	0.1053
LB01-149	1.00E-02	0.4655	0.1267
LB01-021	1.00E-01	0.3137	0.2466
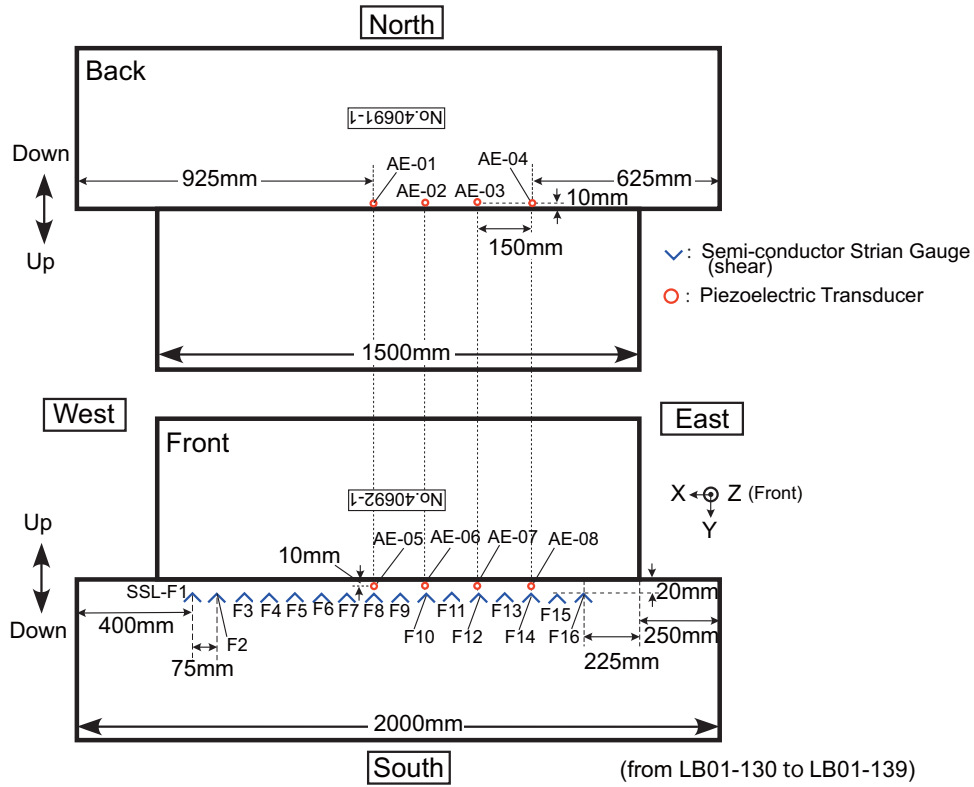
Fig. 13 Locations of PZTs and ST-Ss during the experiments from LB01-130 to LB01-139. Red circles indicate the locations of PZTs and blue hats indicate the locations of ST-Ss. Upper part of the figure is a view from backward of the apparatus and lower is a view from the front.
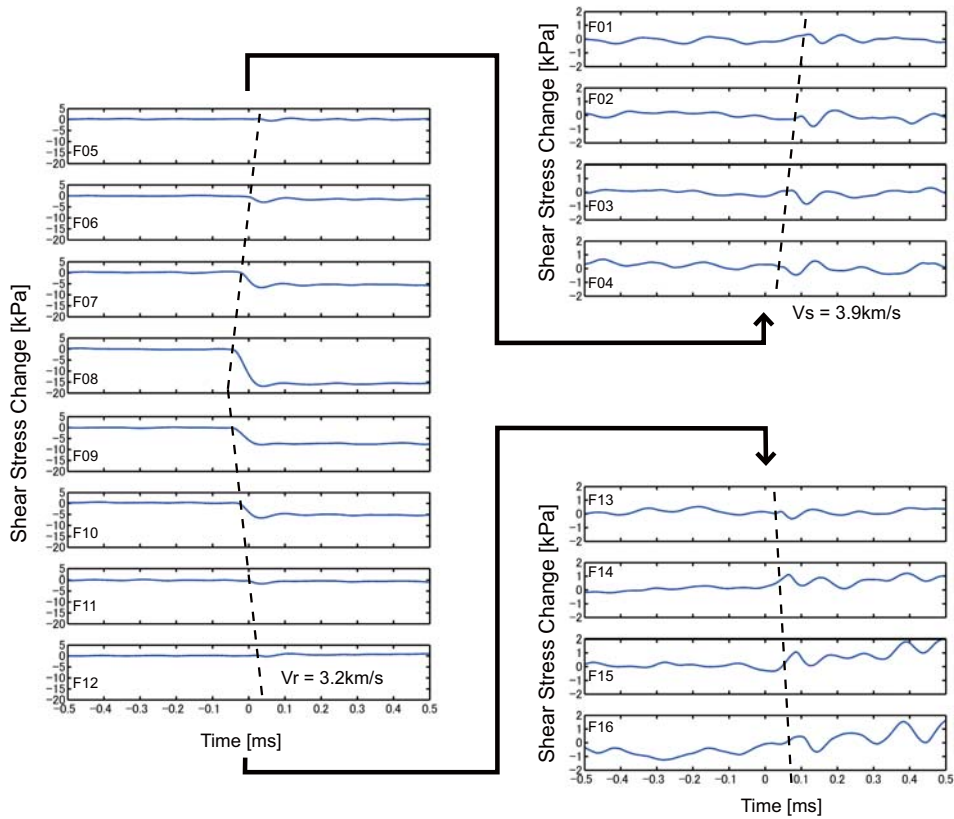
Fig. 14 Stress change during the confined slip event found in the experiment LB01-132 at around 117s from the onset of the slide. The main rupture initiated close to the F08 sensor and propagated bilaterally at a velocity of 3.2 km/s, which is close to the Rayleigh wave velocity. After the termination of the stress drop, elastic shear waves were propagated outside.

As shown in **Fig. 14**, the rupture propagated with Rayleigh velocity and it stopped with a small amount of stress drop. The shear waves propagated outside the ruptured area. It should be noted that the stress drop was the largest at the center of the ruptured area where the rupture was initiated, and it decreased toward the outside. Such a rupture suggests that the stress distribution might be heterogeneous so that a rupture could terminate due to the stress heterogeneity. If the stress is rather uniform, a uniform stress drop is expected because of the rather uniform coefficient of friction.

We also investigated the location of the initiation of the stick-slip rupture. We picked the onset of the waveforms of the PZTs attached to both sides of the fault (**Fig. 15**). The locations of PZTs (AE01-AE08) are shown in **Fig. 13**. As shown in **Fig. 16a**, many stick slip event occurred during a single experiments. To detect the onset of the stick slip events, we first pick the onset of the squared amplitude of the PZT waveforms.

Using the set of arrival time data for each event (**Fig. 15**), we were able to locate the hypocentral locations of the high-frequency source, which should correspond to the initiation points of the dynamic rupture. In this inversion problem, the unknown parameters are the origin times (t_0) and the hypocenter locations (x_0, y_0, z_0) on the sliding surface and the propagation velocity (V). We searched the optimum parameters by a grid search method that minimizes the L^2 norm between the observed and calculated arrival times as shown below.

$$L^2 = \sum_i \left(t_i - t_0 - R_i / V \right)^2 \qquad (1)$$

$$R_i = \sqrt{\left(x_i - x_0 \right)^2 + \left(y_i - y_0 \right)^2 + \left(z_i - z_0 \right)^2} \qquad (2)$$

where t_i is the arrival time measured at i-th station, and (x_i, y_i, z_i) is the location of i-th station. Here, we assume that all hypocenters are on the sliding surface (z_0=0). The results are shown in **Fig. 16b**, where the hypocenters with small ($L < 2.23 \times 10^{-5}$s) and large residuals ($L > 2.23 \times 10^{-5}$s) are plotted with circles and dots, respectively.

We then compared these locations with the surface condition of the sliding fault. The initiation of the rupture tends to occur at the edge of the grooves where new gouge particles are generated during the experiments. We thus speculate that the high stress drop near the rupture initiation is caused by the break of geometrical heterogeneity at the boundary between the unbroken area (shiny surface) and broken area (grooves). It will be interesting to confirm whether the rupture initiation is related to the fault surface geometry in future studies.
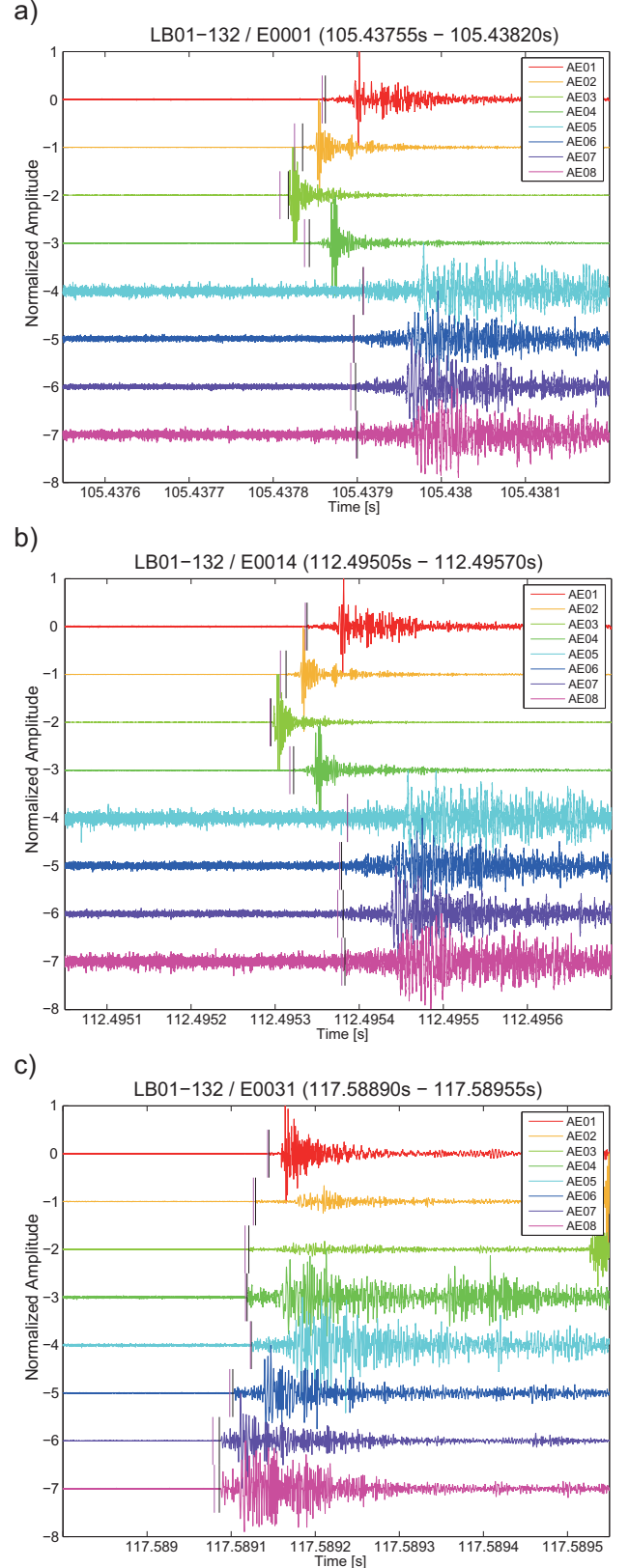
Fig. 15 Some examples of the stick-slip events recorded by PZTs during experiment LB01-132. The black vertical lines are the pick times of the first arrivals, and the purple vertical lines are the expected wave arrival times used for the hypocenter estimated using the pick times.
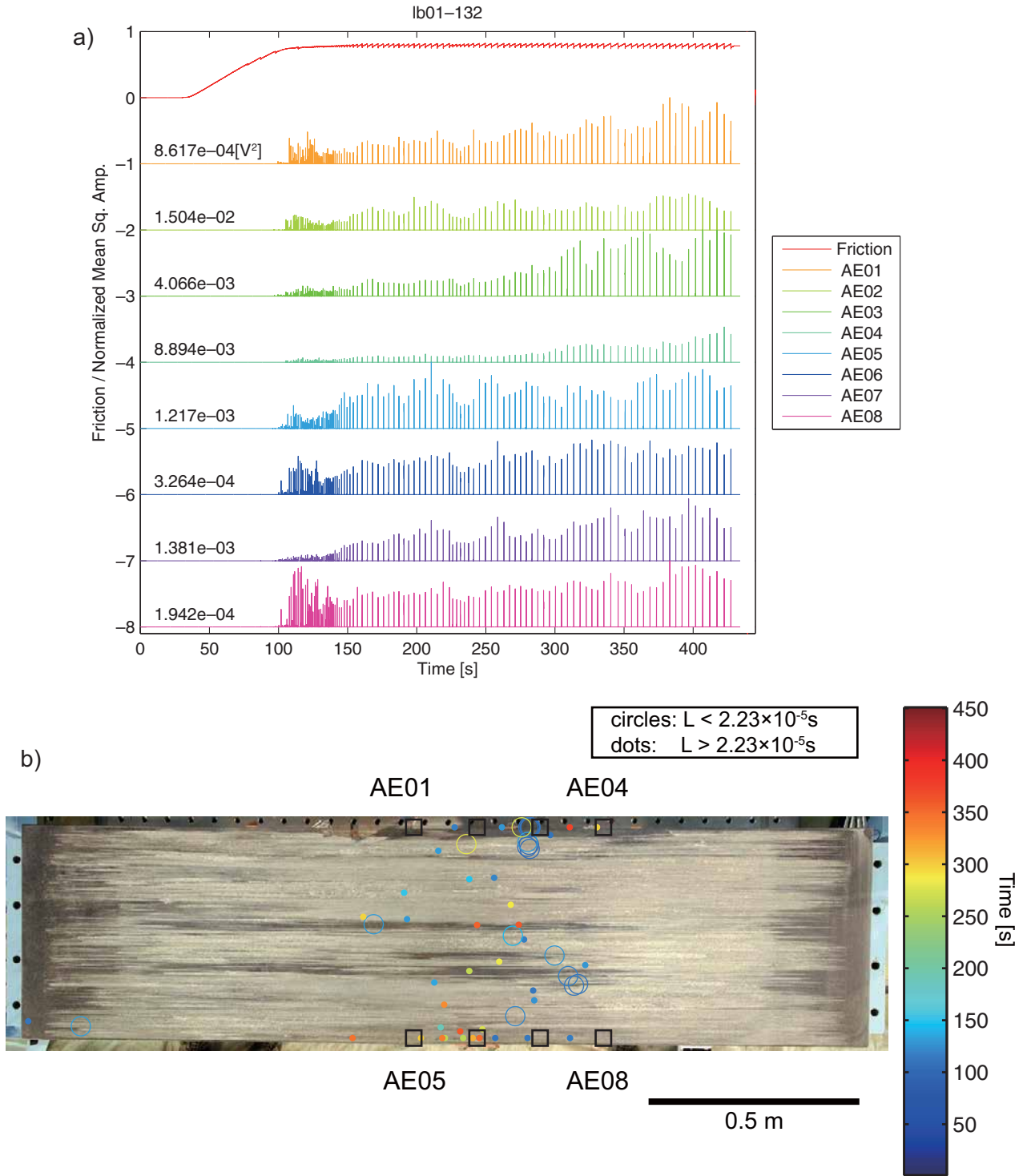
Fig. 16 a) Temporal variation of the coefficient of friction and mean squared amplitudes of PZTs normalized by the maximum amplitude appearing at the beginning of each trace during the experiment LB01-132. **b)** Estimated hypocenter locations are shown by circles (small residuals, $L < 2.23×10^{-5}$s) and dots (large residuals, $L > 2.23×10^{-5}$s) in the experiment LB01-132. Colors correspond to the origin time. Hypocenters are overlaid with the slip surface photograph taken just after the experiment LB01-132; gauge particles were removed from the sliding surface. The light-color portions are grooved areas where gouge particles were created during the experiments. Dark areas correspond to the undamaged areas where the surface becomes shiny due to the grinding. Open squares indicate the location of PZTs.

4. Conclusion

We have developed a large-scale biaxial friction apparatus to investigate the specimen size dependence of friction as well as the characteristics of rupture propagation during coseismic slips (stick slips). The characteristics of this apparatus are 1) its broad range of loading velocity (0.025 mm/s−1 m/s), 2) the large specimen sizes that can be tested (~2 m), and 3) its long displacement (~0.4 m). The stiffness of the apparatus is estimated 0.1 GN/m. Based on the preliminary analysis of the data obtained using the G-1 apparatus, we found that, in principal, size effects of friction seem minor and more detailed investigations are required to extract the size dependence of friction. Especially, the local coefficient of friction close to the sliding surface has not yet been measured. For the stick-slip event analysis, we observed many events that did not propagate until the edge of the specimen. By locating the onsets of these stick slip events, we observed that the rupture seems to be initiated at the edge of the groove where the local geometry of the fault surface is complicated. These observations will help identify the initiation process of natural earthquakes.

Acknowledgements

References

1) Aochi, H. and Fukuyama, E. (2002): Three-dimensional nonplanar simulation of the 1992 Landers earthquake. J. Geophys. Res., **107**(B2), 2035, doi: 10.1029/2000JB000061.

2) Beeler, N., Kilgore, B., McGarr, A., Fletcher, J., Evans, J., and Baker, S. R. (2012): Observed source parameters for dynamic rupture with non-uniform initial stress and relatively high fracture energy. J. Struct. Geol., **38**, 77-89, doi:10.1016/j.jsg.2011.11.013.

3) Byerlee, J. (1978): Friction of Rocks. Pure. Appl. Geophys., **116**, 615-626.

4) Dieterich, J. H. (1972): Time-dependent friction in rocks. J. Geophys. Res., **77**, 3690-3697.

5) Dieterich, J. H. (1978a): Time-dependent friction and the mechanics of stick-slip. Pure Appl. Geophys., **116**, 790-806.

6) Dieterich, J. H. (1978b): Preseismic fault slip and earthquake prediction. J. Geophys. Res., **83**(B8), 3940-3948.

7) Dieterich, J. H. (1979): Modeling of rock friction, 1. Experimental results and constitutive equations. J. Geophys. Res., **84**, 2161-2168.

8) Dieterich, J. H. (1981): Constitutive properties of faults with simulated gouge. Geophysical Monograph, Amer. Geophys. Union, **24**, 102-120.

9) Dieterich, J. H. (1986): A model for the nucleation of earthquake slip. Geophysical Monograph, Amer. Geophys. Union, **37**, 37-47.

10) Dieterich, J. H., Barber, D. W., Conrad, G., and Gorton, Q. A. (1978): Preseismic slip in a large scale friction experiment. Proc. U. S. Rock Mech. Symp., 19th, 110-117.

11) Di Toro, G., Han, R., Hirose, T., De Paola, N., Nielsen, S., Mizoguchi, K,. Ferri, F., Cocco, M., and Shimamoto, T. (2011): Fault lubrication during earthquakes. Nature, **471**, 494-499, doi:10.1038/nature09838.

12) Fukuyama, E. and Mikumo, T. (2006): Dynamic rupture propagation during the 1891 Nobi, central Japan, earthquake: A possible extension to the branched faults. Bull. Seismol. Soc. Am., **96**(4A), 1257-1266, doi:10.1785/0120050151.

13) Fukuyama, E. and Mikumo, T. (2007): Slip-weakening distance estimated at near-fault stations. Geophys. Res. Lett., **34**, L09302, doi:10.1029/2006GL029203.

14) Goldsby, D. L. and Tullis, T. (2011): Flash heating leads to low frictional strength of crustal rocks at earthquake slip rates. Science, **334**, 216-218, doi:10.1126/science.1207902.

15) Guatteri, M. and Spudich, P. (2000): What can strong motion data tell us about slip-weakening fault friction laws?. Bull. Seismol. Soc. Am., **90**(1), 98-116.

16) Hirose, T. and Shimamoto, T. (2003): Fractal dimension od molten surfaces as a possible parameter to infer the slip-weakening distance of faults from natural pseudotachlytes. J. Struct. Geol., **25**, 1569-1574.

17) Hok, S., Fukuyama, E., and Hashimoto, C. (2011): Dynamic rupture scenarios of anticipated Nankai-Tonankai earthquakes, southwest Japan. J. Geophys. Res., **116**, B12319, doi:10.1029/2011JB008492.

18) Koketsu, K., Yokota, Y., Nishimura, N., Yagi, Y., Miyazaki, S., Satake, K., Fujii, Y., Miyake, H., Sakai, S., Yamanaka, Y., and Okada, T. (2011): A unified source model for the 2011 Tohoku earthquake. Earth Planet. Sci. Lett., **310**, 480-487, doi:10.1016/ j.epsl.2011.09.009.

19) Latour, S., Schubnel, A., Nielsen, S. B., Madariaga, R., and Vinciguerra, S. (2013): Characterization of nucleation during laboratory earthquakes, Geophys. Res. Lett., 40, 1-6, doi:10.1002/grl.50974.

20) Lay, T., Kanamori, H., Ammon, C. J., Koper, K. D., Hutko, A. R., Ye, L., Yue, H., and Rushing, T. M.

(2012): Depth-varying rupture properties of subduction zone megathrust faults. J. Geophys. Res., **117**, B04311, doi:10.1029/2011JB009133.

21) Marone, C. (1998): Laboratory-derived friction laws and their application to seismic faulting. Ann. Rev. Earth Planet. Sci., **26**, 643-696.

22) McLaskey, G. C. and Kilgore, B. D. (2013): Foreshocks during the nucleation of stick-slip instability. J. Geophys. Res., **118**, 2982-2997, doi:10.1002/jgrb.50232.

23) Mikumo, T., Olsen, K. B., Fukuyama, E., and Yagi, Y. (2003): Stress breakdown time and slip-weakening distance inferred from slip-velocity functions on earthquake faults. Bull. Seismol. Soc. Am., **93**(1), 264-282.

24) Minowa, C., Ogawa, N., and Ohtani, K. (1989): The report on renewal of large-scale shaking table. Tech. Note Nat'l Res. Inst. Earth Sci. Disas. Prev., **140**, 1-63, http://dil-opac.bosai.go.jp/publication/nied_tech_note/pdf/KJ-01_140.pdf

25) Oglesby, D. D., Archureta, R. J., and Nielsen, S. B. (1998): Earthquakes on dipping faults: The effects of broken symmetry. Science, **280**, 1055-1059.

26) Ohnaka, M. (1973): Experimental studies of stick-slip and their application to the earthquake source mechanism. J. Phys. Earth, **21**, 285-303.

27) Ohnaka, M. (1978): Application of some dynamic properties of stick-slip to earthquakes. Geophys. J. Roy. astr. Soc., **53**, 311-318.

28) Ohnaka, M., Kuwahara, Y., and Yamamoto, K. (1987): Constitutive relations between dynamic physical parameters near a tip of the propagating slip zone during stick-slip shear failure. Tectonophys., **144**, 109-125.

29) Ohnaka, M. and Shen, L.-f. (1999): Scaling of the shear rupture process from nucleation to dynamic propagation: Implications of geometric irregularity of the rupturing surfaces. J. Geophys. Res., **104**(B1), 817-844.

30) Okubo, P. and Dieterich, J. H. (1984): Effects of physical properties on frictional instabilities produces on simulated faults. J. Geophys. Res., **89**(B7), 5817-5827.

31) Reches, Z. and Lockner, D. A. (2010): Fault weakening and earthquake instability by powder lubrication. Nature, **467**, 452-456, doi:10.1038/nature09348.

32) Scholz, C. H. (1968): Microfracturing and the inelastic deformation of rock in compression. J. Geophys. Res., **73**(4), 1417-1432.

33) Shibazaki, B. and Matsu'ura, M. (1998): Transition process from nucleation to high-speed rupture propagation: scaling from stick-slip experiments to natural earthquakes. Geophys. J. Int., **132**, 14-30.

34) Shimamoto, T., Handin, J., and Logan, J. M. (1980): Specimen-apparatus interaction during stick-slip in a triaxial compression machine: A decoupled two-degree-of-freedom model. Tectonophys., **67**, 175-205.

35) Togo, T., Shimamoto, T., Yamashita, F., Mizoguchi, K., and Fukuyama, E. (2014): Stick-slip behavior of Indian gabbro as studied with a NIED large-scale biaxial friction apparatus, submitted to Earthquake Science.

防災科学技術研究所大型振動台を用いた大型二軸摩擦実験
－ 装置の概要と実験結果 －

福山英一[*1]・溝口一生[*2,a]・山下　太[*1]・東郷徹宏[*1,b]・川方裕則[*3,a]・吉光奈奈[*3,c]・
嶋本利彦[*4]・御子柴正[*1]・佐藤　誠[*5]・箕輪親宏[*6,a]・兼澤敏之[*6]・黒川裕士[*6]・佐藤登也[*6]

[*1] 防災科学技術研究所
[*2] 電力中央研究所
[*3] 立命館大学
[*4] 中国地震局地質研究所
[*5] (株) エーイーエス
[*6] (株) 巴技研
[a] 防災科学技術研究所客員研究員
[b] 現在，中国地震局地質研究所
[c] 現在，東京大学地震研究所

要　旨

　岩石摩擦のサイズ依存性と破壊伝播の詳細を調べるため，大型二軸摩擦試験機を開発し，2012 年の春に，防災科学技術研究所所有の大型振動台 (テーブルサイズ 15 m × 14.5 m) を用いて，大型摩擦実験を行った．この実験においては，振動台の起震機を利用して岩石試料間に一定の食い違い速度を与えた．岩石試料は，インド産斑糲岩を用い，長さ 1.5 m の四角柱試料を長さ 2 m の試料に重ねて実験に用いた．各試料の高さと幅はそれぞれ 0.5 m である．下側試料は振動台に固定されており，振動台とともに動く．上側試料は反力バーを介して振動台基礎と接続されている．振動台は, 最大変位 0.4 m, 0.025 mm/s から 1 m/s の速度を出す事ができる．実験に先立って，岩石試料のすべり面は，大型研削盤を用いて凹凸が 0.01 mm 以下になるように整形した．しかしながら，実験回数を重ねるに従い，すべり面の荒さは進化していった．垂直応力は，1.3 MPa までかけて実験を行った．試験機の強度を実験中に測定を行い，0.1 GN/m であった．スティックスリップが顕著に発生しない 0.1 mm/s–1 mm/s の載荷速度における摩擦係数を測定したところ，法線応力が 0.13 〜 1.3 MPa の間において，約 0.75 であり，この値は, 小さいサイズの岩石試料を用いた実験で得られた値とほぼ一致する値であった．さらに, スティックスリップイベントの破壊伝播をひずみゲージアレイを用いて調べ，破壊がすべり面中央部から始まり岩石試料の両端に達しないイベントが多数発生している事がわかった．これらのイベントは，すべり面が摩耗してできた溝の端から始まっている事がわかった．

キーワード : 岩石摩擦実験，大型二軸摩擦試験機，摩擦係数，スティックスリップ，地震破壊伝播